

SHAPE OPTIMIZATION OF BUMPER BEAM UNDER LOW-VELOCITY
IMPACT

by

Sina Dadashzadeh

B.S., Mechanical Engineering, Jābir ibn Ḥayyān University, 2014

Submitted to the Institute for Graduate Studies in
Science and Engineering in partial fulfillment of
the requirements for the degree of
Master of Science

Graduate Program in Mechanical Engineering
Boğaziçi University

2019

ACKNOWLEDGEMENTS

First of all, I would like to express my deep gratitude to my master thesis advisor, Prof. Fazil Onder Sonmez for his endless support, kindness, encouragement and for his precious advice through this work. I have learned not only academic knowledge and skills from him, but also I found him as a real gentle-hearted one.

I would like to mention that this study would not have been possible without the support of my lovely family. Emotional encouragement and nancial support from two angels of my life - My mom and dad -, made my way brighter and more joyful.

I also would like to thank especially to my dear sister Negar and my lovely brothers; Nima, who encouraged me to persue my higher educations and paved the way for me with his valuable thoughts and guidance, and Reza, for his endless support, empathy which made this journey way more delightful. My dissertation is submitted on his 30th birthday so just wanted to say “Happy birthday” to my lovely brother.

At the end, thanks to my friends Sajjad, Shabnam, Hamed, Nima and my lovely officemate, Farzad for their helps and friendship.

ABSTRACT

SHAPE OPTIMIZATION OF BUMPER BEAM UNDER LOW-VELOCITY IMPACT

Bumper beam is an important part of vehicles providing protection from collisions. Its main function is to prevent damage to the rest of the vehicle in low-speed collisions. For this reason, it should absorb the energy of collision at low speeds without undergoing large deflections and large plastic deformation. Weight, cost, and performance are important factors in the design of automotive parts. The objective of this study is to obtain an optimum shape that improves the performance of a bumper beam without increasing weight. The impact phenomenon is simulated in ANSYS LS-DYNA according to IIHS low-velocity impact standard, in which the full-width of the bumper beam hits a rigid barrier by 10 km/h. The objective function to be minimized includes the maximum intrusion as well as the weight. The cross-sectional profile is defined by spline curves passing through key points. The coordinates of the key points are chosen as the optimization variables. The bumper beam is optimized for a steel and an aluminum. Different optimum shapes are obtained for different materials. The two optimum designs and some benchmark shapes are compared in terms of maximum intrusion of the bumper beam, peak transmitted force, maximum plastic strain, weight, and cost. Significant improvements are observed in the performance of the optimally shaped beams compared to the benchmark beams.

ÖZET

DÜŞÜK-HIZLI ÇARPIŞMA ALTINDA TAMPON KİRİŞİNİN OPTİMUM ŞEKİL TASARIMI

Tampon kirişi, araçların çarpışmalardan korunmasını sağlayan önemli bir parçasıdır. Asıl görevi, düşük hızlı çarpışmalarda aracın kalanına oluşacak hasarı engellemektir. Bu sebeple, düşük hızlardaki çarpışmaların enerjisini, büyük sehimlere ve plastik deformasyona uğramadan emmelidir. Ağırlık, maliyet ve performans, otomotiv parçalarının tasarımında önemli etkenlerdir. Bu çalışmanın amacı, tampon kirişinin ağırlığını artırmadan performansını iyileştirmektir. Çarpışmanın benzeşim modeli, ANSYS LS-DYNA’da, IIHS düşük-hızlı çarpışma standardına uygun olarak geliştirildi; bu standarda göre tampon kirişinin tam-genişliği rijit bir bariyere 10 km/sa hızla çarpılmaktadır. Azaltılacak gaye fonksiyonu, maksimum girme miktarının yanı sıra ağırlığı da içermektedir. Enine kesit profili, kilit noktalardan geçen eğrilerle tanımlandı. Kilit noktaların koordinatları eniyileme değişkenleri olarak seçildi. Tampon kirişinin eniyilemesi bir çelik ve alüminyum malzeme için yapıldı. Çeşitli en iyi şekiller farklı malzemeler için elde edildi. İki en iyi tasarım ve bazı kıyaslama şekilleri, tampon kirişinin maksimum girme miktarı, en yüksek iletilen kuvvet, azami plastik gerinme, ağırlık ve maliyet açısından karşılaştırıldı. Diğer kirişlerle karşılaştırıldığında, en iyi şekilli kirişlerin performansında önemli iyileşmeler gözlemlendi.

TABLE OF CONTENTS

ACKNOWLEDGEMENTS	iii
ABSTRACT	iv
ÖZET	v
LIST OF FIGURES	viii
LIST OF TABLES	xi
LIST OF SYMBOLS	xii
LIST OF ACRONYMS/ABBREVIATIONS	xiii
1. INTRODUCTION	1
1.1. Literature Review	2
1.2. Problem Statement	5
1.3. Thesis outline	6
2. LOW-VELOCITY IMPACT STANDARD	7
3. THEORETICAL BACKGROUND	10
3.1. Impact theory	10
3.2. Maximum Distortion Energy Failure Criterion	11
3.3. SMALL AND LARGE DEFORMATION	14
3.3.1. Small deformation theory	14
3.3.2. Large deformation theory	16
3.3.3. Equivalent Plastic Strain	17
3.4. Method	17
3.5. Types of loading	17
3.5.1. Linear vs Non-Linear Behavior	18
3.5.2. Implicit vs Explicit Analyses	18
3.6. MATERIALS	20
3.6.1. Material	20
4. NUMERICAL SIMULATION OF IMPACT	23
4.1. FEA of the Bumper Beam	24
4.2. Boundary and initial conditions of simulation.	26

4.3. ANSYS Parametric Design Language(APDL) commands used to generate the FE model	27
5. OPTIMIZATION PROCEDURE	30
5.1. Introduction	30
5.2. Objective function	30
5.3. Optimization Variables	32
5.4. Modified Simulated Annealing (MSA)	33
6. RESULTS AND DISCUSSIONS	39
6.1. Mesh Convergence Analysis.	39
6.2. Model Validation	40
6.3. Results	45
7. FUTURE WORKS AND RECOMMENDATIONS	55
8. CONCLUSIONS	56
REFERENCES	58
APPENDIX A: HYBRID OPTIMIZATION ALGORITHM	65

LIST OF FIGURES

Figure 1.1.	Common bumper system. [2]	2
Figure 2.1.	Types of frontal impact. [44]	7
Figure 2.2.	Bumper Barrier and Backstop. (b) Barrier and Backstop with Rounded Corners. [45]	8
Figure 2.3.	(a) Right view of the barrier. (b) Top view of the barrier. [46] . .	9
Figure 2.4.	The acceptable region beyond which bumper beam should not deflect.	9
Figure 3.1.	General stress-strain curve. [57]	12
Figure 3.2.	2D geometrical strain deformation. [57]	14
Figure 3.3.	Range of application of implicit and explicit analysis. [48]	19
Figure 4.1.	The cross-sectional profile and area of bumper beam.	24
Figure 4.2.	Shell163 element. [53]	25
Figure 4.3.	The lumped model of bumper beam and rigid barrier.	26
Figure 4.4.	The contact and target nodal components.	27
Figure 4.5.	Cross-section of the bumper beam.	28
Figure 5.1.	Definition of the intrusion.	31

Figure 5.2.	Search region of the moving key points.	32
Figure 5.3.	Order of the objective function values	35
Figure 6.1.	The convergence result of several mesh size.	39
Figure 6.2.	Schematic view of bumper beam for Tanlak's model [62] and the present model.	40
Figure 6.3.	Displacement contour plots of bumper beam in velocity direction obtained by a) Tanlak's model [62], b) the present model.	41
Figure 6.4.	The displacement versus time of the foremost nodes of the two models	42
Figure 6.5.	(a) Initial configurations. (b) Plastic dissipation energy magnitude at 8.2ms . (c) Strain energy magnitude at 8.2ms. [62]	43
Figure 6.6.	Energy diagram obtained by Tanlak's model. [62]	44
Figure 6.7.	Energy diagram for present study.	44
Figure 6.8.	The benchmark and optimum shapes.	45
Figure 6.9.	The intrusion-mass ratio of the steel bumper beams.	46
Figure 6.10.	The intrusion of the steel bumper beams in a same weight situation.	47
Figure 6.11.	The intrusion of the steel bumper beams in various thicknesses.	47
Figure 6.12.	The contour of equivalent plastic strain of the steel bumper beams.	48

Figure 6.13. The energy absorption of the steel bumper beams in a same thickness situation.	49
Figure 6.14. The presence of the plastic hing in steel bumper beams.	50
Figure 6.15. The peak transmitted force at high-velocity impacts for different-shaped beams having the same weight.	50
Figure 6.16. The peak transmitted force at low-velocity impacts for same weight situations	51
Figure 6.17. The Energy absorption of the best shapes in same weight situation.	52
Figure 6.18. The peak transmitted force at low-velocity impacts for the best shapes in same weight situations.	52
Figure 6.19. The intrusion of the best shapes having same weight.	53
Figure 6.20. The contour of equivalent plastic strain of the steel and aluminum best shapes.	53
Figure A.1. The flow-chart of the hybrid-optimization algorithm	65

LIST OF TABLES

Table 3.1.	Explicit and implicit choice criteria (adapted from [48])	19
Table 3.2.	Material Properties of 1018 Steel. [56]	21
Table 3.3.	Material Properties of Aluminum A6061-T6. [52]	22
Table 4.1.	APDL commands for creating key points and lines	27
Table 4.2.	APDL commands for creating areas	28
Table 4.3.	APDL commands for creating mesh	29
Table 4.4.	APDL commands for initial and boundary conditions	29

LIST OF SYMBOLS

A_b	Cross-sectional area
C	Cowper-Symonds strain rate parameters
c_i	Weight coefficient
$[C]$	Damping matrix
E_p	Plastic strain energy
F_{obj}	Objective function
$F(t)$	Load vector
g	gravitational acceleration
$[K]$	Stiffness matrix
$[M]$	Mass matrix
P	Cowper-Symonds strain rate parameters
R_{IM}	gravitational acceleration
t_s	Thickness
u	Nodal displacement vector
W	Weight
W_0	Initial weight
$\dot{\epsilon}$	Strain rate
σ_0	Initial yield stress
σ_y	Yield stress
δ_i	Initial distance
δ_f	Final distance
ρ	Density

LIST OF ACRONYMS/ABBREVIATIONS

2D	Two Dimensional
3D	Three Dimensional
APDL	ANSYS Parametric Design Language
CAE	Computer-Aided Engineering
CFRP	Carbon Fiber Reinforced Polymer
DOF	Degree of Freedom
FDM	Finite Difference Methods
FEA	Finite Element Analysis
FEM	Finite Element Modelling
FRP	Fiber Reinforced Plastic
GFRP	Glass Fiber Reinforced Polymer
GMT	Glass-Mat Thermoplastic
IIHS	Insurance Institute for Highway Safety
MSA	Modified Simulated Annealing
RCAR	Research Council for Automobile Repairs
RSM	Response Surface Model
SA	Simulated Annealing
SMC	Sheet Molding Compound

1. INTRODUCTION

A collision or crash is a sudden occurrence that may cause damage to a vehicle or injury to the occupants. In order to reduce damage to components during collisions and decrease the likelihood of injury, determining the response of the components and designing them to increase their impact resistance and crashworthiness of vehicles are important subjects that draw the attention of researchers.

Low-velocity collisions of vehicles that may occur in a traffic jam and parking lot may cause high damage cost. The main requirements for the vehicle design in low-velocity collisions are limited damage to the front and rear parts of vehicles and low repair cost [1]. Unlike low-velocity collisions, in a high-velocity crash, the cost of repairing the car is ignored; survival of the occupants becomes critical. Accordingly, the requirement for the vehicle design in high-velocity impact is to reduce the likelihood of injury to the occupants.

Bumpers are vehicle parts that play a vital role in reducing the effects of accidents. They have to fulfill both low-velocity and high-velocity impact requirements to provide protection from collisions. As could be seen in Figure 1.1, a bumper system contains stiff and flexible components that serve different purposes. Fascia and energy absorber are flexible components used to reduce injuries to pedestrians at low-velocity impacts. The main function of a bumper beam is to prevent damage to the vehicle in low-speed collisions. For this reason, it should absorb the energy of collision at low speeds in the elastic range with limited plastic deformation [2]; it should also not suffer a large deflection so as not to cause damage to the parts behind the bumper beam like radiator and hood. At high-velocity collisions, stiffer parts behind the bumper beam take the main burden of absorbing the impact energy. Bumper beam, on the other hand, while collapsing in the initial phases of crash helps reducing peak transmitted force, thereby preventing neck injury of the occupants. As an additional requirement in bumper-beam design, it should fit the allocated spacing and should not interfere with other parts [3].

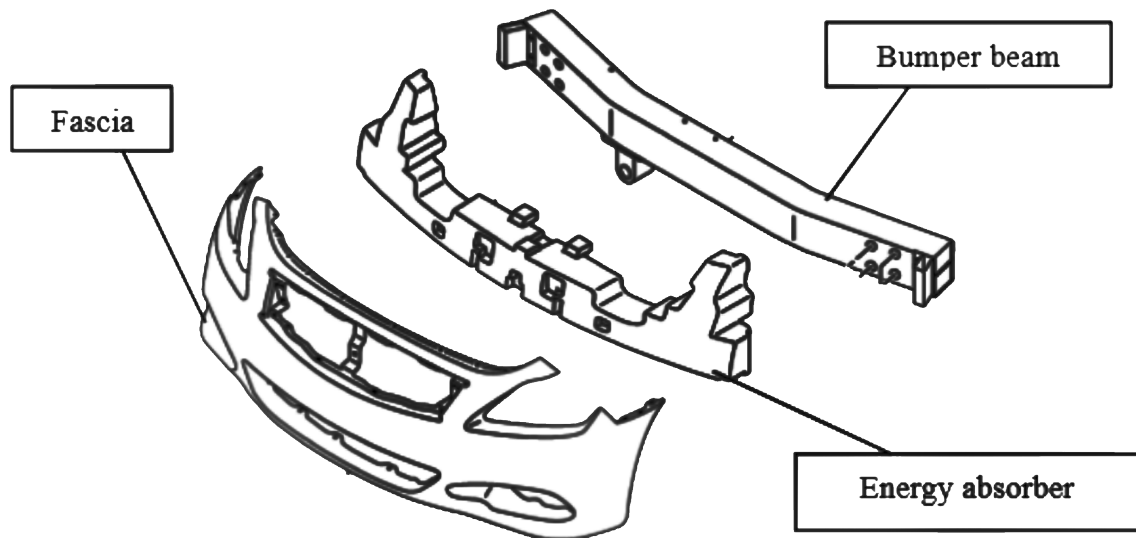


Figure 1.1. Common bumper system. [2]

Another concern in vehicle design is the weight of components. Reducing weight is a way of reducing the material cost, but more importantly, reducing fuel consumption, which means reduced operational cost of vehicles and release of smaller amounts of harmful exhaust gases. For this reason, reduced weight is considered as a design requirement for bumper beams besides high impact resistance. In a bumper design, all the requirements should be satisfied so that satisfactory performance is obtained with limited cost and weight. The important design parameters for bumper beams affecting their energy absorbing capacity are thickness [4], cross-sectional profile [5], overall dimensions [6], longitudinal curvature, strengthening ribs [7], and material. The best way of designing a vehicle part is to conduct an optimum structural design procedure.

1.1. Literature Review

There are a number of studies focusing on the design of bumper beams considering various materials and different shapes.

Zhang *et al.* [6] considered a rib-reinforced thin-walled steel beam that could have a potential use as a bumper beam. The simply supported beam had an impact at its middle with 36 km/h speed. They optimized the shape of the rib by defining a spline curve for its cross-sectional profile. The optimum beam had a lower initial crash force and higher energy absorption characteristics compared to the empty square and foam-filled beams.

Hosseinzadeh *et al.* [8] and Marzbanrad *et al.* [9] compared the impact performance of bumper beams made of glass-mat thermoplastic (GMT), sheet molding compound (SMC), aluminum, and steel. In their FE model, a rigid steel impactor collided the bumper with 4 km/h. They considered the maximum deflection, the maximum impact force, and material failure as performance criteria. Based on the results, they recommended use of SMC, which had advantages like ease of manufacturing due to its simple shape without ribs, use of low-cost composite materials, and lightweight.

Wang *et al.* [10] proposed a lightweight bumper beam design made of carbon-fiber reinforced composite (T300/5208) in order to decrease the weight without compromising on impact resistance. They compared the impact characteristics of steel and composite bumper beams according to low-velocity impact standard ECE R042 [11] the results of that study showed that up to 50% weight reduction is possible using composite materials.

Kokkula *et al.* [12] experimentally and numerically studied the performance of a bumper beam together with crash boxes made of different aluminum alloys in 40%-offset collisions with a speed of $36 \frac{km}{h}$. Numerical predictions and test results correlated well.

Farkas *et al.* [13] considered 40%-offset impact against a rigid barrier at $16 \frac{km}{h}$ as well as impact against a rigid pole at $15 \frac{km}{h}$. They optimized the shape of a bumper beam for minimum mass and maximum energy absorption using DoE (design of experiments) and RSM (response surface model). They imposed constraints on the maximum intrusion and the maximum impact force.

Cheon *et al.* [14] estimated cross-sectional dimensions and thickness of a composite bumper beam from the strength requirements. In their FE model, they applied an equivalent static force evaluated based on deceleration curve obtained from frontal collision test of a car. They also performed tests on bumper beams under static bending load to validate their model. They concluded that a composite bumper beam with a weight of about 30% of steel one had about the same bending strength.

Belingardi *et al.* [15] considered central-frontal impact of a bumper beam on a rigid barrier at $15 \frac{km}{h}$. They compared various cross-sectional profiles, different beam curvatures, and different materials including composites and steel in terms of failure, peak impact force, and maximum displacement. The results showed that E-glass/epoxy pultruded bumper beam had better progressive failure behavior with reduced peak load compared to other materials.

Li *et al.* [16] studied the maximum intrusion and the energy absorption ratio of bumper beams considering central-frontal collisions at $4 \frac{km}{h}$ and $8 \frac{km}{h}$ and oblique collision at $2.5 \frac{km}{h}$. The authors verified their FE model using a drop hammer impact test. They selected a suitable thickness so that the bumper beam satisfied the performance requirements of the tests.

Fuhao Mo *et al.* [17] investigated the effects of an impactor colliding a bumper system at $8 \frac{km}{h}$ simulating central-frontal collision and a legform impactor at $40 \frac{km}{h}$ simulating pedestrian impact. They optimized the geometry of the bumper using design of experiments considering both pedestrian safety and low-speed impact resistance of the bumper.

Yim *et al.* [18] considered collision of a steel bumper beam on a rigid wall and also a rigid pole at $5 \frac{km}{h}$. They optimized the cross-sectional dimensions to minimize the weight without violating the maximum intrusion constraint. They used response surface modeling (RSM) to reduce the computational time.

Wang and Li [10] investigated the effects of a rigid impactor colliding on a bumper at $4 \frac{km}{h}$. They chose a suitable thickness for the bumper beam so that it satisfied the requirements for the maximum intrusion, the maximum Von Mises stress, and energy absorption. They found that the bumper beam made of carbon-fiber-reinforced composite had better impact performance compared to steel beam with 50% less weight.

Sonawane and Shelar [19] used a full car model to simulate central frontal impact on a rigid barrier at $10 \frac{km}{h}$ and corner impact at $5 \frac{km}{h}$. They tried different values of thickness and different shapes for a steel bumper beam to increase absorbed energy and limit maximum intrusion.

The previous studies on bumper beam design considered central-frontal [20], offset frontal [13, 21, 22], pole [3, 23, 24] and corner [25] collisions. They chose different types of materials, steel [10, 26, 27], aluminum [25, 28], carbon-fiber reinforced polymer [10], glass-fiber [28, 29] and reinforced polymer [30]. Some studies [8, 9, 25] compared the impact resistance of bumpers made of different materials. A number of researchers [3, 13, 31–33] optimized bumper beam under low-velocity impact conditions. However, the past studies mainly concentrated on size and thickness optimization except for a few topological [23, 32] and shape [3, 31] optimization studies. Some other researchers used cross-sectional dimensions [12, 34] [13, 38] as optimization variables. As performance criteria for bumper beams subjected to low-velocity impact, they used the maximum intrusion [10, 16, 19, 35–39], energy absorption [29, 40–42] and peak impact force [3, 15, 43].

1.2. Problem Statement

In this study, a methodology is developed to optimize cross-sectional shape of bumper beams considering their mechanical response in a standard low-velocity central collision test. A multi-objective function is formulated that includes the weight of the bumper beam and the maximum intrusion. The cross-sectional profile is defined by spline curves passing through key points. The coordinates of the key points are taken as design variables in the optimization process. The optimum values for the coordi-

nates leading to minimum objective function value are obtained using a hybrid search algorithm, which is a combination of Modified Simulated Annealing and Nelder-Mead algorithms. Peak transmitted force during collisions is another performance parameter for bumper beams. This is not considered during optimization, but comparisons are made between the optimum shape and benchmark shapes regarding peak force.

1.3. Thesis outline

In chapter 2, starting with a brief introduction to the standard collision test, the requirements on the performance of the bumper beam in this scenario are explained. In chapter 3, the theories used in this study about failure criteria and impact phenomena explained, also, focuses on the materials and the type of analysis used in this project. The modeling and simulation of the impact scenario, which are done by developing codes in ANSYS-APDL, are described in chapter 4. The optimization process and the objective function is explained in detail in Chapter 5. In chapter 6, The validation of the FEM model is described and the results and discussions comes in this chapter. In the end the chapter 7 and 8 are covering the future work recommendation and the conclusion respectively.

2. LOW-VELOCITY IMPACT STANDARD

The collision scenarios considered in the design of vehicles are frontal impact, rear impact, side impact, and roof impact. Frontal impact is considered in this study, because front bumper beam is affected only in this test case. There are three types of frontal impact; Full frontal collision, offset frontal collision, and pole frontal collision as shown in Figure 2.1 [44]. In this study, the bumper beam is design for the loading conditions in full frontal collision.

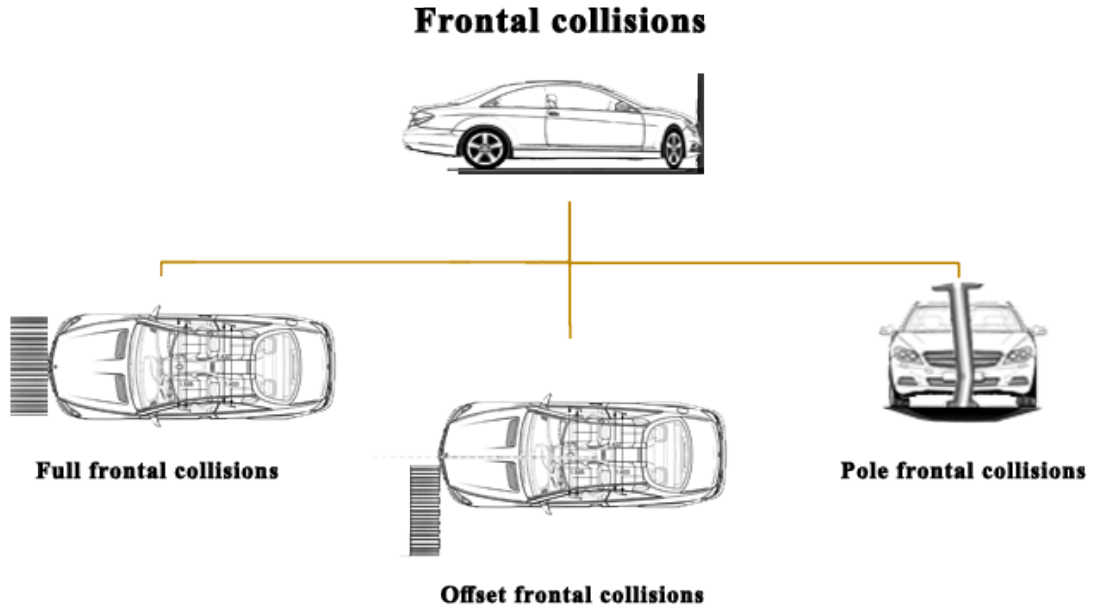


Figure 2.1. Types of frontal impact. [44]

There are a number of standards for low-velocity collision tests. Among them, the low-velocity impact standard of the Insurance Institute for Highway Safety (IIHS) [45] is selected. The response of the bumper is simulated considering the impact conditions in the standard and the requirements for bumper beams in this standard are taken as the quality requirements for the design of the bumper beam. The rigid obstacle made

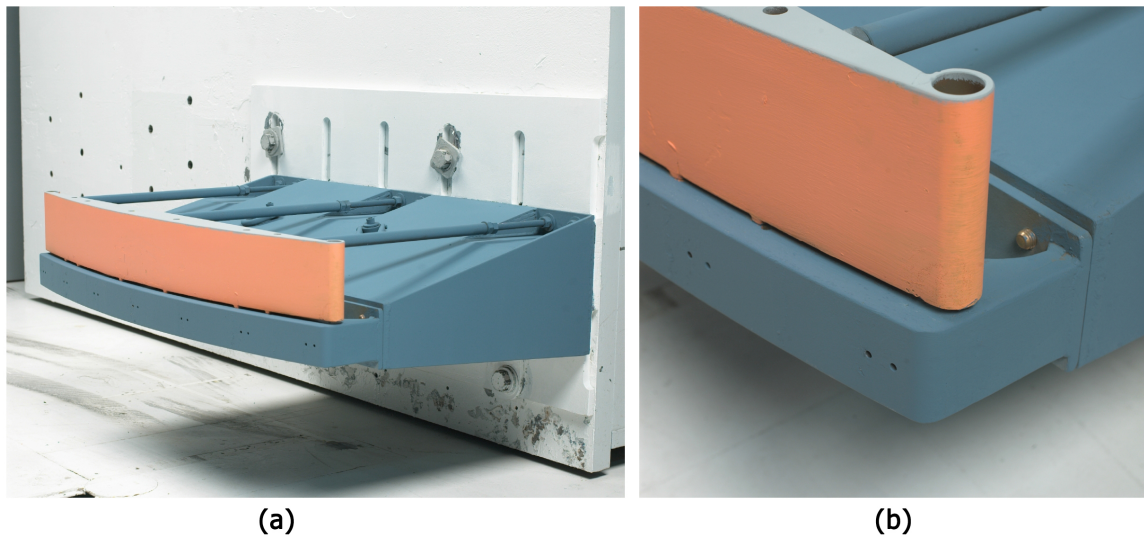


Figure 2.2. Bumper Barrier and Backstop. (b) Barrier and Backstop with Rounded Corners. [45]

of A-36 hot rolled steel used in this standard as shown in Figure 2.2.

The IIHS impact test is used to determine the behavior and energy dissipation capacity of the various vehicles in low-velocity collisions. There are some limitations for the design of bumper beams. IIHS encourages all the manufacturers to follow those limitations in order to produce more stable bumpers and solve the drawbacks like under-ride and over-ride phenomenon [46]. These phenomena occur when two vehicles do not have an in-line bumper beam to hit each other. Hence, one goes under or over the others. The risk of under-ride/over-ride in low-velocity crashes will be decreased by using standard heights for bumper beams in order to make it in alignment with other vehicles to avoid high repair costs [46].

According to the IIHS, the test conditions are as follows:

- The height of the installed barrier from the ground to the lower edge is 457mm. (Figure 2.3)
- The impact velocity is $10 \frac{km}{h}$.
- The barrier height is 200 mm.

- The radius of the rigid barrier is 3404 mm.

Tested vehicles should not suffer any serious damage



Figure 2.3. (a) Right view of the barrier. (b) Top view of the barrier. [46]

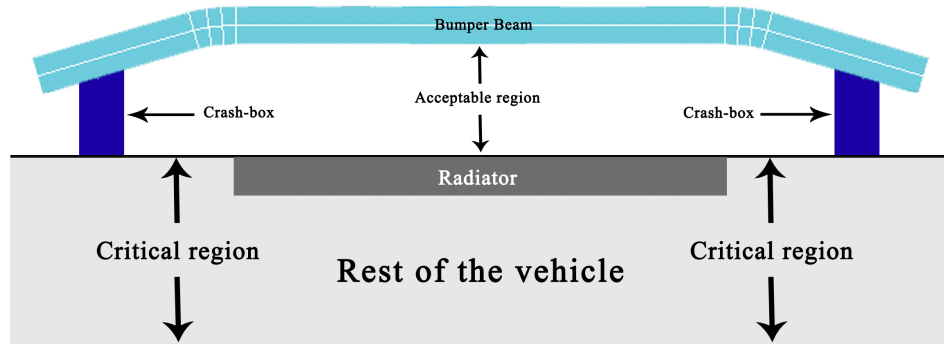


Figure 2.4. The acceptable region beyond which bumper beam should not deflect.

according to the low-velocity impact standards [8, 9, 20]. In order to avoid damage to the components behind the bumper beam, the deflection of the bumper beam should be limited so that it will not penetrate into the critical region shown in the Figure 2.4.

3. THEORETICAL BACKGROUND

3.1. Impact theory

There are two types of impacts: Elastic impact and plastic impact. These two types of impacts differ in their energy dissipating capability. In an elastic impact, there is no permanent deformation due to the energy transferred between the two collided bodies. In contrast, a plastic impact occurs with permanent deformation, if the transferred energy exceeds the energy absorbing capability of the material in elastic range. In a case of frontal collisions, the impact type is elasto-plastic depending on the speed of collision. At the beginning, there is just kinetic energy in system which depends on the mass and the velocity of the vehicle. As can be seen in Eq. 3.1, the general forms of energy includes kinetic energy (E_K), gravitational potential energy (U_g), elastic—plastic—strain energy (U_s), and heat (E_H).

$$E_{Ki} + U_{gi} = E_{Kf} + U_{gf} + U_{sf} + E_{Hf} \quad (3.1)$$

in which, E_{Ki} and E_{Kf} denote the initial and final kinetic energy of the vehicle, and the subscript i and f indicate the initial and final situations of the mentioned energies. In this study, the thermal energy and other types of energies like sound energy are not considered. Assuming the remaining elastic strain energy of the vehicle is small, most of the energy absorption of the system is done by plastic deformation . By subtracting the initial and final kinetic energy of system, E_p , plastic strain energy can be expressed as follow:

$$E_p = \frac{1}{2}m(V_i^2 - V_f^2) \quad (3.2)$$

3.2. Maximum Distortion Energy Failure Criterion

This failure criterion says that the yielding failure occurs when a distortion energy exceeds or be equal to the maximum distortion energy of the material in the tensile test. The strain energy is composed of two distinct forms – volume changes and distortion (angular change). Normal strains cause a change in volume, shear strain cause distortions. The total strain energy is the sum of distortion energy and volume energy:

$$U_{total} = U_{distortion} + U_{volume} \quad (3.3)$$

where:

U_{total} = total strain energy

$U_{distortion}$ = strain energy due to distortion

U_{volume} = strain energy due to volume change (a.k.a hydrostatic strain energy)

We will develop equations for total strain energy (U_{total}) and volume energy (U_{volume}), and determine the distortion energy (which is really what we are interested in) from:

$$U_{distortion} = U_{total} - U_{volume} \quad (3.4)$$

Remember, for uniaxial loading, the strain energy per unit volume is the area under the stress-strain curve (Figure 3.1), for general (3D) loading, the total strain energy is given in terms of principal stresses and strains:

$$U_{total} = \frac{1}{2}[\epsilon_1\sigma_1 + \epsilon_2\sigma_2 + \epsilon_3\sigma_3] \quad (3.5)$$

Using Hooke's law $\epsilon_1 = \frac{1}{E}[\sigma_1 - \nu(\sigma_2 + \sigma_3)]$ etc. the total strain energy Eq. 3.5 can be

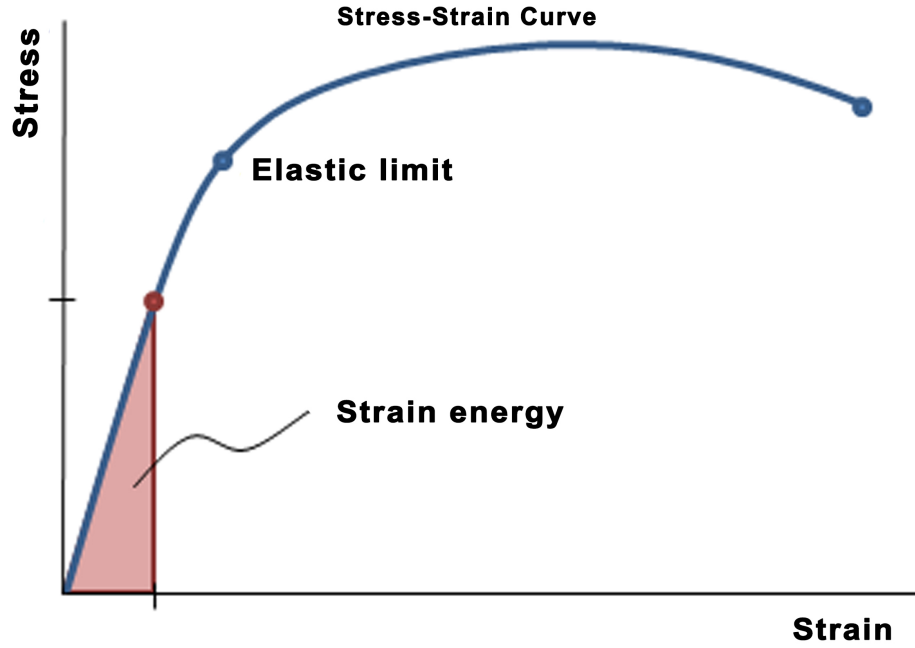


Figure 3.1. General stress-strain curve. [57]

written in terms of stress only:

$$U_{total} = \frac{1}{2E}[\sigma_1^2 + \sigma_2^2 + \sigma_3^2 - 2\nu(\sigma_2\sigma_3 + \sigma_1\sigma_3 + \sigma_1\sigma_2)] \quad (3.6)$$

Remember that hydrostatic stress causes volume changes and that it is invariant (hydrostatic stress is a scalar – it is not directionally dependent – therefore it does not vary depending upon axis orientation). “Invariant” means “does not vary.” The hydrostatic stress can be determined from the average magnitudes of the three principal stresses:

$$\sigma_{hydrostatic} = \sigma_{ave} = \frac{\sigma_1 + \sigma_2 + \sigma_3}{3} \quad (3.7)$$

$\sigma_{hydrostatic}$ is the stress condition that causes volume change.

$$\begin{aligned} U_{volume} &= (3(1 - 2\nu)/2E)\sigma_{hydrostatic}^2 \\ &= (3(1 - 2\nu)/2E)((\sigma_1 + \sigma_2 + \sigma_3)/3)^2 \\ &= ((1 - 2\nu)/6E)(\sigma_1^2 + \sigma_2^2 + \sigma_3^2 + 2\sigma_2\sigma_3 + 2\sigma_1\sigma_2 + 2\sigma_1\sigma_3) \end{aligned} \quad (3.8)$$

By substituting Eq. 3.6 and 3.8 into Eq. 3.4;

$$U_{distortion} = \frac{1}{2E}(\sigma_1^2 + \sigma_2^2 + \sigma_3^2 - 2\nu(\sigma_2\sigma_3 + \sigma_1\sigma_2 + \sigma_1\sigma_3)) - \left(\frac{1-2\nu}{6E}\right)(\sigma_1^2 + \sigma_2^2 + \sigma_3^2 + 2\sigma_2\sigma_3 + 2\sigma_1\sigma_2 + 2\sigma_1\sigma_3) \quad (3.9)$$

Simplifying Eq. 3.9 gives:

$$U_{distortion} = \frac{1+\nu}{6E}[(\sigma_1 - \sigma_2)^2 + (\sigma_2 - \sigma_3)^2 + (\sigma_3 - \sigma_1)^2] \quad (3.10)$$

So, If the distortion energy be equal or exceeds the distortion energy of the material in uniaxial test, failure occurs:

$$U_{distortion,part} \geq U_{distortion,uni-axial} \quad (3.11)$$

Equating the distortion energy in general 3-dimensional stress condition in part (Eq.3.10) and distortion energy in simple uniaxial loading (Eq.3.12):

$$U_{distortion,uni-axial} = \frac{1+\nu}{3E}\sigma_{sy}^2 \quad (3.12)$$

from equations (3.10) and (3.12) into equation (3.11):

$$\frac{1+\nu}{6E}[(\sigma_1 - \sigma_2)^2 + (\sigma_2 - \sigma_3)^2 + (\sigma_3 - \sigma_1)^2] \geq \frac{1+\nu}{3E}\sigma_{sy}^2 \quad (3.13)$$

Simplifying equation (Eq. 3.13) gives the von Mises failure criterion:

$$If \quad \frac{1}{2}[(\sigma_1 - \sigma_2)^2 + (\sigma_2 - \sigma_3)^2 + (\sigma_3 - \sigma_1)^2] \geq \sigma_{sy}^2 \quad (3.14)$$

then yielding will occur.

3.3. SMALL AND LARGE DEFORMATION

3.3.1. Small deformation theory

Figure 3.2 shows a rectangular element with initial dimension of $dx \cdot dy$ where, the dotted shape indicates the deformed shape of it. The point A is a point on undeformed rectangle which located at (x, y) , then, after deformation the displacement of corresponding point are $u(x, y)$ and $v(x, y)$. The displacement of point B are $u(x+dx, y)$

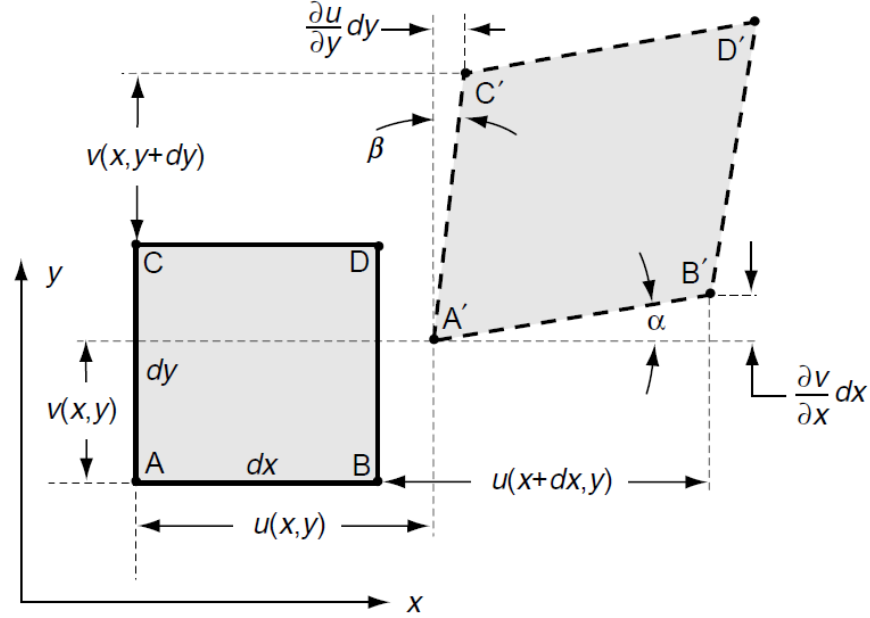


Figure 3.2. 2D geometrical strain deformation. [57]

and $v(x+dx, y)$, and the displacement of the other points are defined in a same manner. The statement $u(x + dx, y) \approx u(x, y) + (\frac{\partial u}{\partial x})dx$ follows small deformation theory [47] with similar expansions for all other terms. The normal strain in x-direction can be defined by

$$\epsilon_x = \frac{A'B' - AB}{AB} \quad (3.15)$$

Accordingly, the length of the $A'B'$ calculated as,

$$A'B' = \sqrt{\left(dx + \frac{\partial u}{\partial x}dx\right)^2 + \left(\frac{\partial v}{\partial x}dx\right)^2} = \sqrt{1 + 2\frac{\partial u}{\partial x} + \left(\frac{\partial u}{\partial x}\right)^2 + \left(\frac{\partial v}{\partial x}\right)^2}dx \quad (3.16)$$

$$\approx \left(1 + \frac{\partial u}{\partial x}\right)dx$$

where the higher-order terms dropped in order to consistent with small deformation theory. By substituting Eq. 3.16 into Eq. 3.15 and taking $AB = dx$, the strain in x-direction reduces to,

$$\epsilon_x = \frac{\partial u}{\partial x} \quad (3.17)$$

similarly, in y and z direction becomes,

$$\epsilon_y = \frac{\partial v}{\partial y} \quad (3.18)$$

$$\epsilon_z = \frac{\partial w}{\partial z} \quad (3.19)$$

As shown in Figure 3.2, changing in angles leads to make another types of strain called shear strain. In small deformation, $\alpha \approx \tan\alpha$ and $\beta \approx \tan\beta$, so shear strain can be expressed as

$$\gamma_{xy} = \frac{\frac{\partial v}{\partial x}dx}{dx + \frac{\partial u}{\partial x}dx} + \frac{\frac{\partial u}{\partial y}dy}{dy + \frac{\partial v}{\partial y}dy} = \frac{\partial u}{\partial y} + \frac{\partial v}{\partial x} \quad (3.20)$$

By considering similar behaviour in the y-z and x-z planes, the results extended to general 3D case as,

$$\epsilon_x = \frac{\partial u}{\partial x}, \epsilon_y = \frac{\partial v}{\partial y}, \epsilon_z = \frac{\partial w}{\partial z} \quad (3.21)$$

$$\gamma_{xy} = \frac{\partial u}{\partial y} + \frac{\partial v}{\partial x}, \gamma_{yz} = \frac{\partial v}{\partial z} + \frac{\partial w}{\partial y}, \gamma_{zx} = \frac{\partial w}{\partial x} + \frac{\partial u}{\partial z} \quad (3.22)$$

These six independent components of strain, completely describe small deformation theory. These results are written in engineering strain components where the finite element method prefers to use the strain tensor e_{ij} . As there is only a minor change because the normal strains are identical and shearing strains are one-half; using the tensor strain, the strain-displacement realations expressed as,

$$e_x = \frac{\partial u}{\partial x}, e_y = \frac{\partial v}{\partial y}, e_z = \frac{\partial w}{\partial z} \quad (3.23)$$

$$e_{xy} = \frac{1}{2} \frac{\partial u}{\partial y} + \frac{\partial v}{\partial x}, e_{yz} = \frac{1}{2} \frac{\partial v}{\partial z} + \frac{\partial w}{\partial y}, e_{zx} = \frac{1}{2} \frac{\partial w}{\partial x} + \frac{\partial u}{\partial z} \quad (3.24)$$

the general form of tensor strain will becomes to

$$e_{ij} = \frac{1}{2}(u_{i,j} + u_{j,i}) \quad (3.25)$$

3.3.2. Large deformation theory

On the other hand, when the strains in a material exceed more than a few percent, the changing geometry due to this deformation can no longer be neglected. Analyses which include this effect are called large strain, or finite strain, analyses. It is also important to note that the plastic strains in a solid depend on the load history. This means that the stress-strain laws are not just simple equations relating stress to strain. Instead, plastic strain laws must either relate the strain rate in the solid to the stress and stress rate, or else specify the relationship between a small increment of plastic strain de^p_{ij} in terms of strain, stress and stress increment $d\sigma_{ij}$. While a solid underwent a large deformation, the yield stress may increase during plastic straining, so in section 3.6.1 will see that the yield stress is a function of a measure of total plastic strain.

3.3.3. Equivalent Plastic Strain

The equivalent plastic strain gives a measure of the amount of permanent strain in an engineering body. The equivalent plastic strain is calculated as,

$$\epsilon_{eqv} = \frac{1}{1 + \nu'} \sqrt{\left(\frac{1}{2}\right)(\epsilon_1 - \epsilon_2)^2 + (\epsilon_2 - \epsilon_3)^2 + (\epsilon_3 - \epsilon_1)^2} \quad (3.26)$$

where ν' is effective Poisson's ratio, which is defined as 0.5 for plastic strains.

3.4. Method

There is no analytical solution for many engineering problems, such as problems with complex geometry or loading conditions. Therefore, analytical methods have limited applicability. However, problems with complex geometry and loading conditions can be analyzed numerically. To solve such problems, there are many numerical methods, such as finite element method (FEM), boundary element method, finite difference methods (FDM), non-mesh methods, and so on. Among the existing numerical methods, finite element method is the most commonly used method for solving complex problems. Among the large variety of FE software, ANSYS can be used to solve problems of highly nonlinear and transient nature. Accuracy and precision are the requirements for achieving acceptable results using finite element software.

3.5. Types of loading

The type of loading is one of the most important factors in structural problems. The loads are mainly classified as static and dynamic. In problems with static loading condition, the sum of all applied forces and moments are zero so the structure is under equilibrium. On the other side, there are problems involving dynamic loads; as the name implies, the load is dynamically applied and unlike static loading, it is depending on time. Vehicle collision tests pose a dynamic problem. In such problems, static approach does not make sense, because velocity and inertia of the vehicle considerably

affect the behavior of the whole structure, so the problem should be treated as fully dynamic. The equation of motion for transient dynamics in FEA can be written as

$$[M]\left\{\frac{d^2u}{dt^2}\right\} + [C]\left\{\frac{du}{dt}\right\} + [K]\{u\} = \{F(t)\} \quad (3.27)$$

where $[M]$ is the mass matrix, $[C]$ is the damping matrix and $[K]$ is the stiffness matrix [48].

3.5.1. Linear vs Non-Linear Behavior

As both static and dynamic problems can be treated as linear or non-linear, after knowing the types of loading, it is important to evaluate whether the deformation behavior of the structure is linear or nonlinear. Linear behavior of structure means that stresses are proportional to strain and deflection of the structure is small enough to consider the change in geometry insignificant. The linear behavior should only be used in problems with small deflection. Non-linear behavior of structures always comes up in problems involving contact of deformable parts and plastic deformation. In a crash analysis, due to existence of contacts and possible plastic deformation, the material model is highly non- linear [48].

3.5.2. Implicit vs Explicit Analyses

After recognizing the behavior of the structure, one may need to find the best numerical formulation to solve the problem accurately. Both implicit and explicit solvers can solve the problems with non-linear behavior (Figure 3.3), none of them has the priority to other, it means that there are some limitations for both of them. About the suitability of implicit and explicit methods for the problem at hand, Table 3.1 presents some criteria.

Table 3.1. Explicit and implicit choice criteria (adapted from [48])

Implicit Non-Linear Analysis	Explicit Non-Linear Analysis
Long events (few seconds)	Short events (milliseconds)
Small deformation	Large deformation
Less number of contacts	Complex and large number of contacts
Simple material models	Wide variety of material options

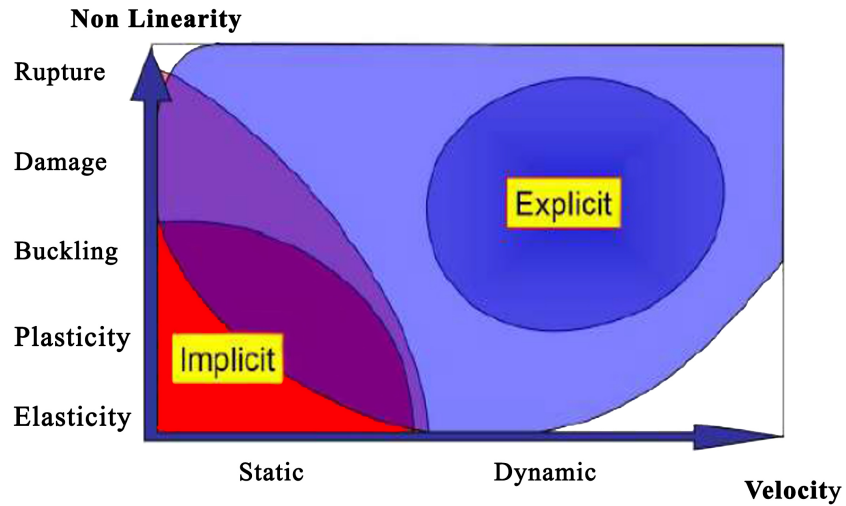


Figure 3.3. Range of application of implicit and explicit analysis. [48]

In this study, the total time of the impact is less than 80 milliseconds, the deformation is large within an acceptable region, the contacts are complex and the material is selected to behave non-linearly. Considering the criteria mentioned in Table 3.1, the obvious choice is to use an explicit non-linear analysis which can accurately simulate the real collision.

3.6. MATERIALS

3.6.1. Material

In recent years, reducing the weight of vehicle in order to reduce greenhouse gases and fuel consumption has gained significance. There is considerable research on finding feasible material and shape for bumper systems. Some researches were interested in finding a composite material to be used in bumper beams, e.g. glass-fiber reinforced plastics [2,7], carbon-fiber reinforced plastic (T300/5208) [10], thermoplastic olefin elastomers denoted with TPO [3]. This is because composites have a potential to significantly reduce the weight of vehicles. Hambali *et al.* [7] compared three types of thermoset matrices by applying the TOPSIS method. The materials such as epoxy resins, polyester and vinyl ester are chose as the candidate for the hybrid bio-composites. Among them, vinyl ester resin was the best thermoset matrix to be used in the development of hybrid bio-composite automotive bumper beam component.

Hernandez *et al.* [49] used inverse characterization technique to understand the behavior of the selected test material, low carbon steel AISI 1018. Table 3.2 shows the mechanical properties of the selected material. For ensuring the homogeneity of results, the test specimens they used in their study have the same cold drawn rod of 4.75mm in radius. In low-velocity impact, it requires to evaluate the plastic behavior of the part so plastic kinematic model selected as a constitutive material model with only kinematic hardening [50]. This elastoplastic model shows the stress-strain behavior of the material via a bilinear model, which is dependent on strain rate, having its basis on Cowper-Symonds constitutive model, [51], within which Elastic Modulus E outlines the slope up to the initial yield point. In this material model, yield stress σ_y calculated using Equation 3.28 as:

$$\sigma_y = \sigma_0 \left[1 + \left(\frac{\dot{\epsilon}}{C} \right)^{\frac{1}{P}} \right] \quad (3.28)$$

where, σ_0 denotes the initial yield stress, $\dot{\epsilon}$ signifies the strain rate, and C and P are representing the Cowper-Symonds strain rate parameters. Additionally, the tangent slope of the stress-strain curve after elastic portion stands for the strain hardening behavior as Tangent Modulus, E_{tan} . Consequently, this constitutive model requires six parameters to be characterized. These six parameters, as mentioned above, are: the modulus of elasticity E, the initial yield stress σ_0 , the tangent modulus E_{tan} , the Cowper-Symonds parameters C and P and at the end the Poisson's ratio which are defined in Table 3.2 [56]. According to the low-velocity impact standards, the model should not undergo too much plastic deformation, so we need to investigate the plastic deformation and put some penalty in the objective function. Therefore, nonlinear plastic kinematic material 1018 Steel is defined for the bumper beam. The material properties of 1018 Steel are given in Table 3.2.

Table 3.2. Material Properties of 1018 Steel. [56]

Parameters	Values	Units
Elastic Modulus, E	210e3	Pa
Poisson's Ratio, ν	0.27	-
Density	7800	Kg/m^3
Yield Stress	370e6	Pa
Tangent Modulus	763e6	Pa
C(Cowper-Symonds strain rate parameters)	40	S^{-1}
P (Cowper-Symonds strain rate parameters)	5	-
Failure Strain	0.27	-

Beside the steel material, the same material model applied to Aluminum A6061-T6. The material properties and the Cowper-Symonds parameters of A6061-T6 is given in Table 4.2 [52].

Table 3.3. Material Properties of Aluminum A6061-T6. [52]

Parameters	Values	Units
Elastic Modulus, E	70e9	Pa
Poisson's Ratio, ν	0.33	-
Density	2700	Kg/m^3
Yield Stress	252e6	Pa
Tangent Modulus	600e6	Pa
C(Cowper-Symonds strain rate parameters)	25000	S^{-1}
P (Cowper-Symonds strain rate parameters)	0.95	-
Failure Strain	0.17	-

4. NUMERICAL SIMULATION OF IMPACT

Numerical methods along with analytical and empirical ones help to solve engineering problems by simulating physical systems. In this study, the structural analysis of the bumper beam is carried out using commercial finite element software, ANSYS, which is a powerful CAE software that can carry out complex engineering analyses by its variety of contact algorithms, time-based loading features, and nonlinear material models. ANSYS is capable of analyzing the problems in the field of impact, explosion, and transient loading at various speeds. With the help of this software, one can analyze linear, geometrically non-linear problems including large displacements, and materially nonlinear problems including plastic deformation. The finite element model of the bumper beam is constructed in following order:

- Initialization of the program
- Defining the material properties
- Defining the geometrical parameters
- Defining the key points
- Constructing the geometry of the bumper beam and the barrier
- Creating the FE mesh
- Coupling the mass point with the bumper beam
- Applying the boundary conditions
- Obtaining the solution

To begin with, the type of analysis is selected as “structural with LS-DYNA Explicit.” The properties of the material like the modulus of elasticity, Poisson’s ratio, and density are defined (given in Table 3.2 and 3.3). After generating the key points, the spline curves are defined passing through them. Since the model in this thesis is 3D, by extruding the lines through drag lines, the areas of the geometry are created. Then, the areas are meshed with the user-defined mesh size which is determined by mesh convergence analysis. Subsequently, the boundary constraints, the types of contact, and the initial velocity are defined and the slave nodes are coupled to master one

(mass point). The following sections discuss the details of the aforementioned steps.

4.1. FEA of the Bumper Beam

In this section, the modeling of the bumper beam is explained. Two different materials are chosen for the beam, which are 1018 Steel and AA6061-T6 Aluminum having the material properties given in Chapter 3.6. The cross-sectional profile of the bumper beam is defined using spline curves passing through key points (Figure 4.1). The geometry of the beam is symmetric about X-Y and X-Z planes. Accordingly, the key points are positioned symmetrically. The areas of the geometry are created by extruding the lines defining the cross-sectional profile through drag lines (Figure 4.1).

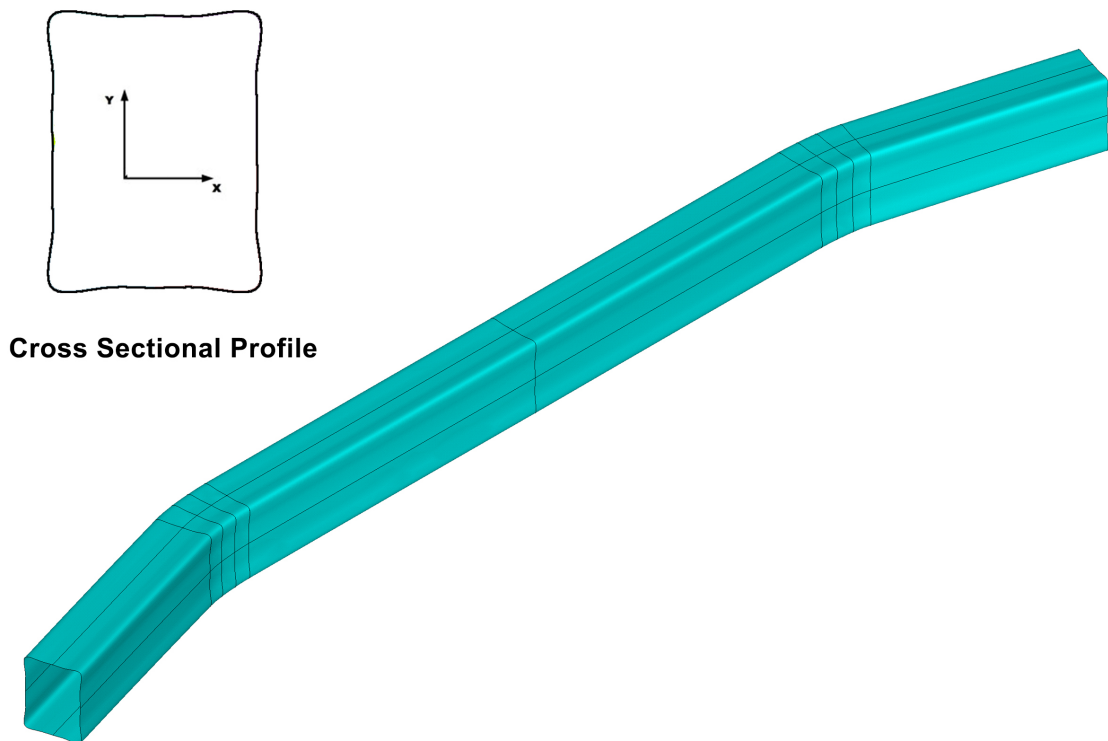


Figure 4.1. The cross-sectional profile and area of bumper beam.

After areas are created, finite element meshes are generated using a shell element, Shell163. This is a 3D explicit thin structural 4-node element with both bending and membrane capabilities. The nodes are indicated as I, J, K, L as shown in Figure 4.2 [53]. Each node has three translational and three rotational degrees of freedom.

Shell elements are used to model the structural response of the bumper beam, because its thickness is much smaller than the lateral dimensions. The main advantage of using shell elements is reduced computational cost compared to solid elements due to the reduced number of finite elements. Besides, the post-processing is faster in large models. The barrier is also created using Shell163 element.

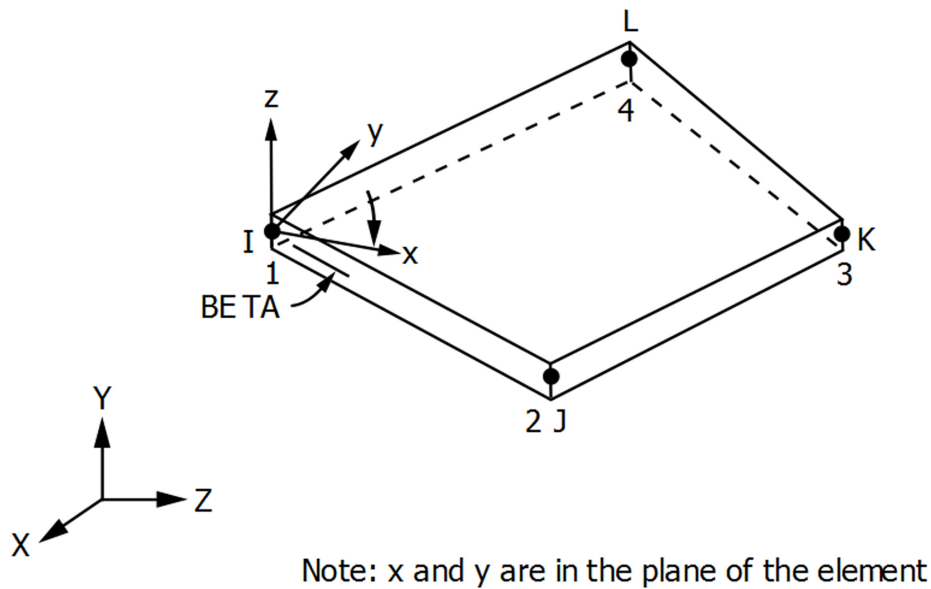


Figure 4.2. Shell163 element. [53]

Figure 4.3 shows the rigid wall and bumper structure. Energy absorbing capacity of the soft parts like fascia and energy absorber is assumed to be negligible in low-velocity collisions. While bumper beams are subjected to transverse loads, crash boxes are mainly subjected to axial loads. As a result, deformation is much larger in bumper beam compared to crash boxes in low-velocity impacts. As one study [61] indicated the bumper beam underwent significant plastic deformation while deformation in the crash boxes mainly remained elastic in a velocities under $10 \frac{Km}{h}$. For these reasons, in this study, the whole impact energy is assumed to be absorbed by the bumper beam in low-velocity collisions. Neglecting the effect of other parts in absorbing the impact energy is a conservative assumption in bumper beam design, because the bumper beam will absorb less energy in collision tests and suffer less deformation compared to simulation results. The rest of the vehicle including crash boxes is modelled as mass points attached to the bumper beam. The element used for mass points is Mass166. This

is a point element which has three translational degrees of freedom with concentrated mass components ($\frac{Force*Time^2}{Length}$) in the element coordinate directions about the element coordinate axes. In this study, according to the standard, the whole weight of the vehicle is 1100 Kg; accordingly 550 kg mass is defined for each of the two nodal points.

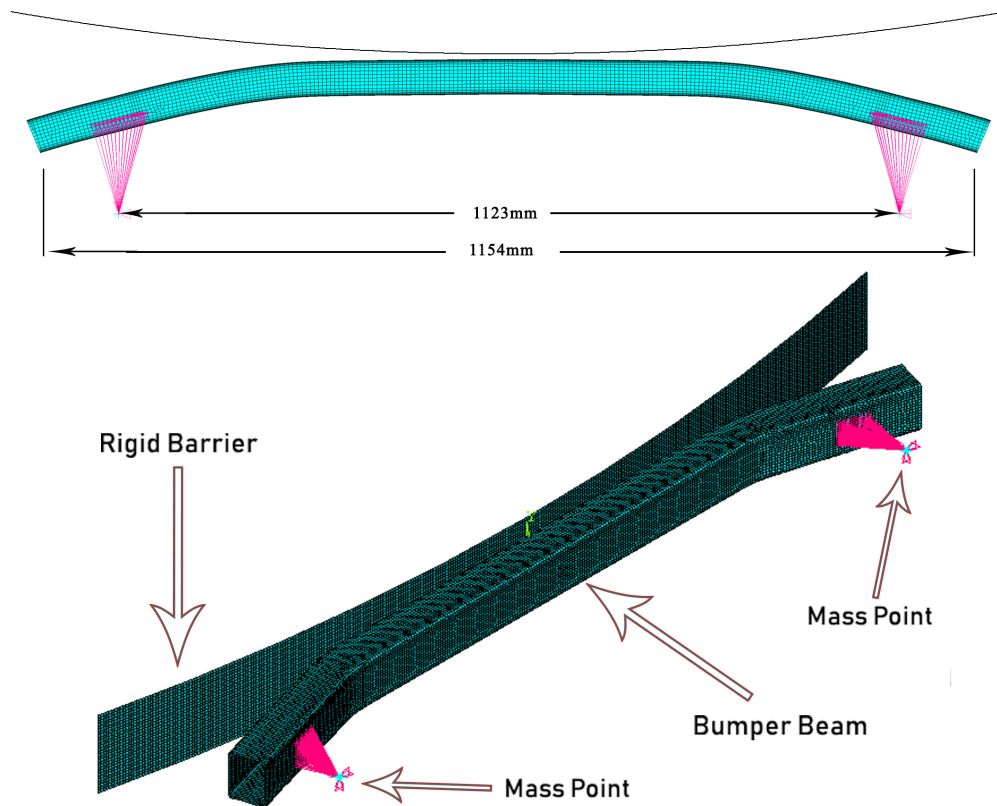


Figure 4.3. The lumped model of bumper beam and rigid barrier.

4.2. Boundary and initial conditions of simulation.

In the FE model, the barrier is rigid with all degrees of freedom constrained at each node. Rigid bodies do not undergo any deformation. The bumper beam moves at an initial speed of $2.78 \frac{m}{s}$ ($10 \frac{km}{h}$) and hits the barrier with this speed. The mass points are constrained in all degrees of freedom except translational movement in the x direction. The contact between the barrier (rigid wall) and the bumper beam is defined as automatic surface-to-surface. Accordingly, contact and target surfaces are

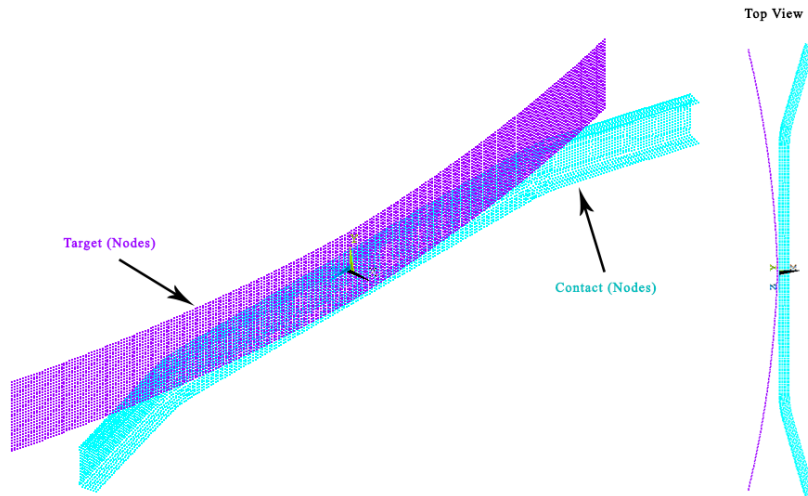


Figure 4.4. The contact and target nodal components.

defined as nodal components (Figure 4.4). Also, there is another contact defined for bumper beam known as self contact (single surface contact) where the both contacts are penalty based with friction coefficient of 0.2.

4.3. ANSYS Parametric Design Language (APDL) commands used to generate the FE model

Key points and lines are created by APDL codes. The descriptions of the commands are given in table 4.1.

Table 4.1. APDL commands for creating key points and lines

Command	Description
$X_{r_{kp}} = val1$	The x coordinate of key point, rkp is the number of related key point, val1 is the value of the x coordinate.
$Y_{r_{kp}} = val2$	The y coordinate of key point, rkp is the number of related key point, and val2 is the value of the y coordinate.
$K, r_{kp}, X_{r_{kp}}, Y_{r_{kp}}$	The key point, rkp, is created.
$bspline, r_{kp1}, r_{kp2}, r_{kp3}$	Spline curves through key points rkp1-3 created.

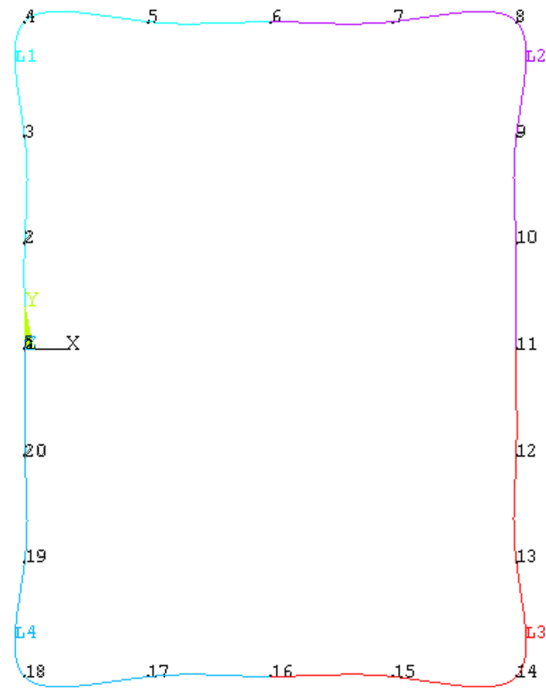


Figure 4.5. Cross-section of the bumper beam.

After the cross section of the bumper beam created using key points and spline curve commands, the areas of the model are created using the commands in Table 4.2.

Table 4.2. APDL commands for creating areas

Command	Description
<i>adrag, P1, , , , , P2</i>	P1 is the selected lines to extrude, P2 is the drag line of the extrusion.
<i>aglu, all</i>	Merging the non-contacted areas together.

After creating the areas, SHELL163 elements are generated on the areas using free-mapped quadratic elements. The results of the FE analysis depend on the size of these elements, so, mesh convergence applied to the model to find the best size fit to the model. Besides, the regions which are important in the results should accurately

meshing using Mesh Refinement. The commands used for mesh are given in table 4.3.

Table 4.3. APDL commands for creating mesh

Command	Description
<i>Lesize, all, elemsize</i>	Size of the elements defined by “elemsize”.
<i>Amesh, Bumper</i>	“Bumper” is the area components to be meshed.
<i>Lsel, s, line, , l₁, l_n</i>	Mesh refinement applied on lines between l_1 and l_n .
<i>Lrefine, all, , , qr</i>	“qr” is the quantity of mesh refinement, takes a value between 1 and 5 (minimum to maximum refinement).

As explained Table 4.4, transitional and rotational constraints are imposed on some lines and nodes using boundary condition commands. Velocity is defined for the nodes of the bumper beam and mass points as initial condition.

Table 4.4. APDL commands for initial and boundary conditions

Command	Description
<i>Dl, Lbr, all</i>	Constraining all DOF of the all lines of barrier.
<i>D, massr, , ROTY, 0</i>	The rotational move of node, massr in Y direction is fixed to zero.
<i>D, massl, , ROTY, 0</i>	The rotational move of node, massl in Y direction is fixed to zero.
<i>D, massr, , ROTZ, 0</i>	The rotational move of node, massr in Z direction is fixed to zero.
<i>D, massl, , ROTZ, 0</i>	The rotational move of node, massl in Z direction is fixed to zero.
<i>EDVE, VELO, BumpB, Vin</i>	Initial velocity of bumper beam, Vin, applied to the bumper beam.
<i>EDVE, VELO, MPN, Vin</i>	Initial velocity of Mass Points, Vin, applied to the mass points.

5. OPTIMIZATION PROCEDURE

5.1. Introduction

The aim of the design optimization is to find the best acceptable configuration according to the constraints and requirements of the problem. In each problem, there are many different solutions; comparison of them and selection of the optimum are done using a function called objective function. The choice of this function depends on the nature of the problem. For example, weight or cost is one of the main goals of structural optimization of vehicles. Selecting an appropriate objective function is one of the most important steps in optimization. In this thesis, a hybrid optimization used to find the optimum shape and weight for the bumper beam. To speed-up the optimization process, combination of Modified Simulated Annealing (MSA) and Nelder-Mead algorithms are used. First, the region within the solution domain that is likely to contain the globally optimum design or a near-global optimum design is found using the global search algorithm MSA, then to find the global optimum shape, the optimization process is continued using a local search algorithm called Nelder-Mead.

5.2. Objective function

In this study, a multi-objective function is adopted. The objective function includes both the weight of the bumper beam and the maximum intrusion. The search algorithm tries to minimize the objective function by trying different values for the design variables. The main requirement from a bumper beam undergoing low-velocity collision is limited deflection, or intrusion, to prevent damage to the components behind the bumper beam like radiator. For this reason, the extent of intrusion is also included in the objective function. As shown in Figure 5.1, the intrusion is defined as the change in the distance between the displacements of the middle backside of the bumper beam and the mass points (representing the rears of the crash-boxes) and calculated as Eq 5.1.

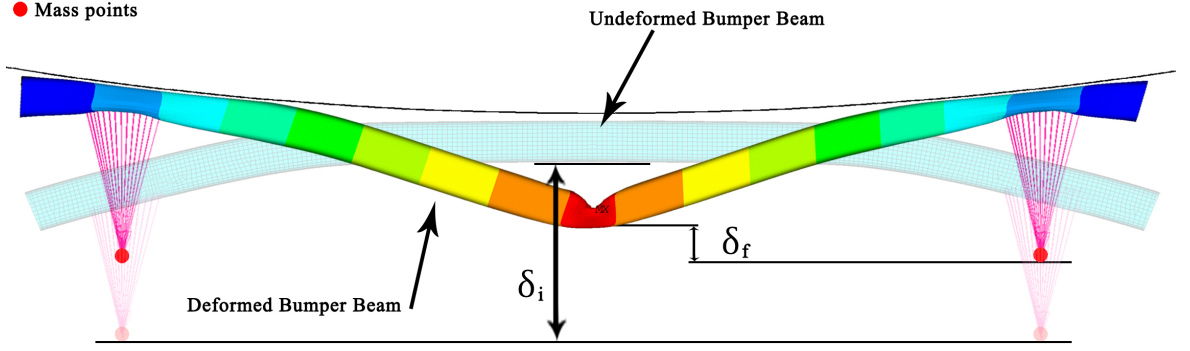


Figure 5.1. Definition of the intrusion.

$$I = \delta_i - \delta_f \quad (5.1)$$

where δ_i and δ_f are the initial and last distance between the rear of the crash boxes and the back of the bumper beam. Accordingly, the objective is formulated as

$$F_{\text{obj}} = c_1 \frac{W}{W_0} + c_2 \frac{I}{I_0} \quad (5.2)$$

where W and I are the weight and the maximum intrusion of the current configuration generated by the search algorithm. W_0 and I_0 are the weight and the maximum intrusion of the beam with rectangular cross-section, where the weight is calculated as Eq 5.3. Because these two variables have different units, they are normalized. c_i are constant weight parameters. In this way, a multi-objective optimization problem is defined. The optimization procedure minimizes both weight and intrusion. By choosing different values for c_i , one may give more importance to one of the terms.

$$W = \rho g t_s A_b \quad (5.3)$$

where, ρ is the density of the material ($\frac{kg}{m^3}$), g , gravitational acceleration ($\frac{m}{s^2}$), t_s is the thickness of the bumper beam (m) and A_b is the cross-sectional area of the bumper beam (m^2).

5.3. Optimization Variables

In this thesis study, the metal bumper beam is considered to be manufactured by a process like extrusion; for this reason, the shape of the cross-section is taken as constant along its length. The curvature of the bumper beam, despite its effect on intrusion, is not considered in this study. Only the cross-sectional shape of the bumper beam is optimized. The cross-section of the bumper beam is defined using spline curves passing through key points. Accordingly, the coordinates of the moving key points are taken as optimization variables.

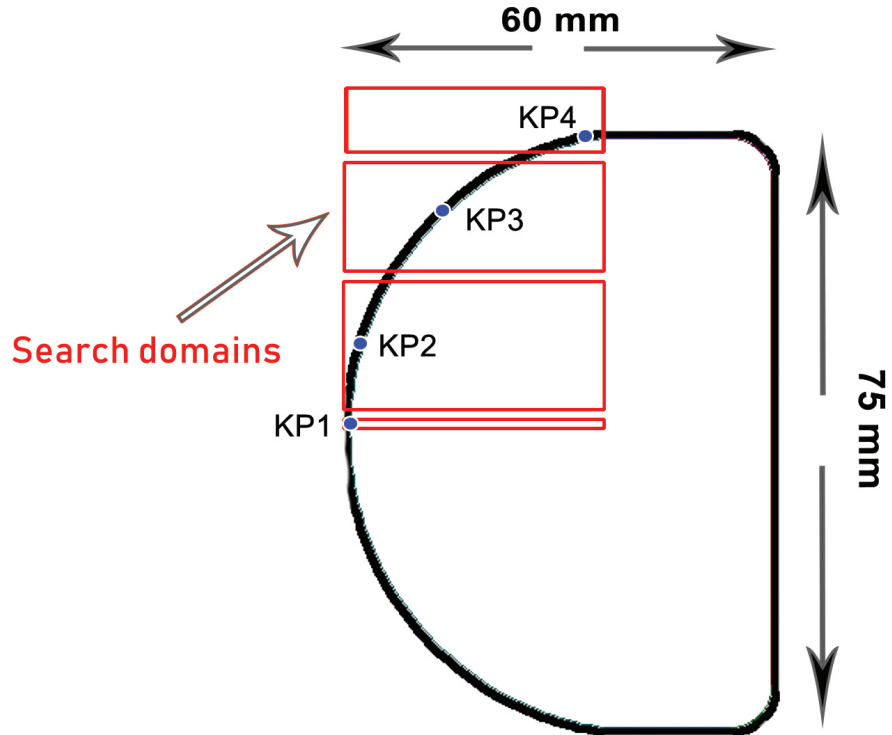


Figure 5.2. Search region of the moving key points.

Figure 5.2 shows a dome cross-section with seven optimization variables. The key point one (KP1) is restricted to move only in x-direction because of the symmetry about x-z plane; where, other six points are free to move in both x and y directions. Each of the points are allowed to move in a defined region which called search domain. As the coordinates of the key points are changed, a new shape is generated. The key points in the symmetric part of the cross-section have the same coordinates as their counterparts. The optimum shape for the bumper beam is obtained by determining the optimum positions of the key points via the optimization process. Only the front part of the cross-section is optimized, because the back end of the bumper beam is attached to the rest of the vehicle through crash-boxes and those parts have specific designs. Moreover, the thickness of the wall is not considered as an optimization variable, but optimum shapes can be obtained for different values of thickness to achieve desired weight reduction.

5.4. Modified Simulated Annealing (MSA)

The optimum shape of the metal bumper beam is found using Modified Simulated Annealing (MSA) which is proposed by M. Akbulut and F. O. Sonmez [54]. Considering that x and y coordinates of the moving key points are optimization variables, the number of design variables is given as

$$n = 2 (n_f - n_r) \quad (5.4)$$

where n_f and n_r are the number of free key points and the number of restricted key points, respectively. Because there are four moving key points and only key point 1 is restricted to move in the x direction, the number of optimization variables is seven. The new shape is obtained, whenever the positions of the moving key points are changed. By randomly changing the values of x and y coordinates of the moving key points, a new configuration is generated. In each iteration, first a configuration is randomly selected from the set of current configurations. The X'_k and Y'_k are the coordinates of the Kth moving key point of the selected configuration, their new values

are calculated as

$$X'_k = X_k + C_r R_{\max} \cos(\theta_r) \quad (5.5)$$

$$Y'_k = Y_k + C_r R_{\max} \sin(\theta_r) \quad (5.6)$$

where X_k and Y_k , indicated the coordinates of the Kth moving key point of the randomly selected configuration, C_r , randomly takes a value in $(0,1)$, R_{\max} is the maximum distance that key points can move, θ_r is a randomly selected value between 0 and 2π . At least one moving key point is needed for shape optimization. The precision of the optimization depends on how the design variables defined in optimization system. The number of key points used in an optimization process is important such that a low number of them quickly leads to an optimal solution, whereas, using a high number of key points leads to a more precisely defined optimal shape, but at the expense of more computational time.

There exists a set of current configurations updated in each iteration during the optimization process. Their number, N , is selected based on the number of design variables, n , as

$$N = 8 \times (n + 1) \quad (5.7)$$

Unlike the standard simulated annealing (SA), this algorithm keeps a set of current configurations instead of just one. Good configurations are kept in the set; if a newly generated configuration is accepted, it replaces one of the worse ones.

After initial configurations are randomly generated, their objective function values are calculated after carrying out finite element structural analysis, where, the weight and the intrusion of the bumper beam calculated. The intrusion is calculated in all the time points and the maximum value is selected among them as the maximum intrusion

of the generated configuration.

The objective function value of a newly generated configuration, F_{obj} is calculated using Equation 5.2. Its acceptability is evaluated according to the following criterion:

$$\mathcal{A}_t = \begin{cases} 1 & , F_{obj} \leq F_h \\ \exp\left(\frac{F_h - F_{obj}}{T_k}\right) & , F_{obj} > F_h \end{cases} \quad (5.8)$$

where F_h is the objective function value of one of the worst current configurations (the configuration indicated by “c” in Figure 5.3). If a new configuration has a lower objective function value than F_h , it is accepted. Otherwise, acceptance of the configuration depends on the acceptability, A_t , which is calculated using Equation 5.8 and compared with a randomly generated number (R_t) between 0.0 and 1.0

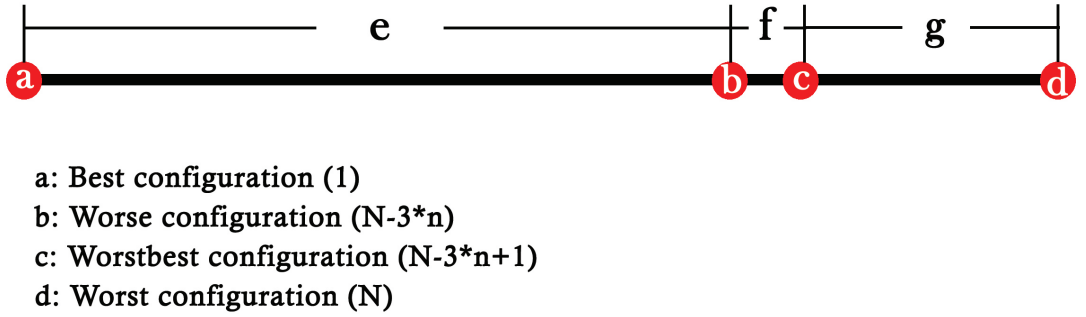


Figure 5.3. Order of the objective function values

$$R_t = \begin{cases} Accepted & if A_t \geq R_t \\ Rejected & if A_t < R_t \end{cases} \quad (5.9)$$

If the trial design is accepted according to Equation 5.9 it replaces a randomly selected current configuration having objective function value larger than the worse configu-

ration (the configurations between the worst-best and worst configurations, indicated as “c” and “d” in Figure 5.3). The configurations between best and worse configurations (indicated as “a” and “b” in Figure , thus, remain in the current configuration. In each iteration, the current configurations are ordered, accordingly, the objective function values of the best, worse, worst-best, and worst configurations are updated.

The probability of acceptance is controlled by a temperature parameter, T_k . In the beginning of the optimization, while T_k has high values, a worse configuration having a higher cost is more likely to be accepted. At the initial stages of optimization, a high value is assigned to the temperature parameter T_0 , so that almost any new configuration regardless of its cost is accepted (as implied in Equation 5.8). Using high temperature for starting the optimization process leads to the search of the entire domain. The set of configurations that are generated at a given temperature is called Markov chain (inner loop). Minimum length of Markow chain depends on the number of design variables as

$$Lt = 3n \quad (5.10)$$

$$Lt_c = \text{nint} \left(Lt \left(1 + 2 \left(\frac{rs}{rs_{in}} \right) \right) \right) \quad (5.11)$$

According to Equation 5.11, the length of Markow chain depends on the step size ratio, which indicates that as the step size ratio approaches to 0, the length of Markow chain becomes equal to Lt , while at the start it is equal to $3n$. where Lt_c is the length of current Markow chain, *nint* is an APDL command which finds the nearest integer to the value within the parenthesis, rs and rs_{in} are the current and initial step size (0.008 m), respectively. The selection of the initial step size, rs_{in} , depends on the search domain. If the F_{obj} is less than the best configuration (Point “a”) during an inner loop , the current loop is closed and a new one starts. If the F_{obj} is less than the worse configuration (point ”b”), this means that there is an improvement in the part of

the current configurations that are not replaced after a new configuration is accepted. The number of the improvements is counted according to

$$N_{im} = N_{im} + 1 \quad (5.12)$$

where N_{im} is the number of improvements in an inner loop. If N_{im} is less than 10% of the number of trials, the step size, rs , is reduced as

$$rs = 0.9 * rs \quad (5.13)$$

As a final stage of Markow chain, the temperature is decreased using the following criterion :

$$R_a = \frac{A_m}{in} \quad (5.14)$$

In which, R_a is the ratio of the accepted movements and A_m is the number of the accepted point.

$$R_s = \left(\frac{rs}{rs_{in}}\right) + 0.01 \quad (5.15)$$

That R_s is the step size ratio,

$$\begin{cases} \alpha = \alpha_{min} & \text{if } R_a > R_s \\ \alpha = \alpha_{max} & \text{if } R_a < R_s \end{cases} \quad (5.16)$$

where, α is the decrement constant for temperature and α_{min} and α_{max} are 0.9 and 0.9999, respectively. There is only one condition for the temperature to remain constant, which means that Lt_n is not equal to Lt_c , in that case $\alpha = 1$. At the end, the worse and the best configurations will be compared, if the current temperature is less than a very small value 5e-04 and the difference between the objective function values of the worse and the best configuration is less than 5e-08, the optimization process is stopped; otherwise the temperature is again decreased as

$$ck = alfa * ck \quad (5.17)$$

After finding an acceptable shape that follows all the criterion and limitations, the iteration of optimization process continues with Nelder-Mead algorithm to ensure that the optimum value is global. As the Nelder-Mead algorithm is a well-known optimization algorithm, the optimization process does not included in the thesis contents and just the flow-chart of the algorithm comes in Appendix A.

6. RESULTS AND DISCUSSIONS

6.1. Mesh Convergence Analysis.

In this study, the finite element method which is an approximate solution technique used to obtain the results, so, the resulting errors should be less than an acceptable limit. One of the ways to ensure that the results have acceptable accuracy is mesh-convergence analysis. The deflection of front node of bumper beam selected to compare with Tanlak's results [62]. As shown in Figure 6.1, the element size of $5 \times 5 \text{ mm}^2$ shows a nearest results to Tanlak's result. So, a suitable size for the finite elements in the grid structure determined. In the explicit analysis of the impact, quadratic elements are used. The shape of the element is chosen as rectangular, but the software generates triangular elements in areas where quadratic mesh cannot be generated.

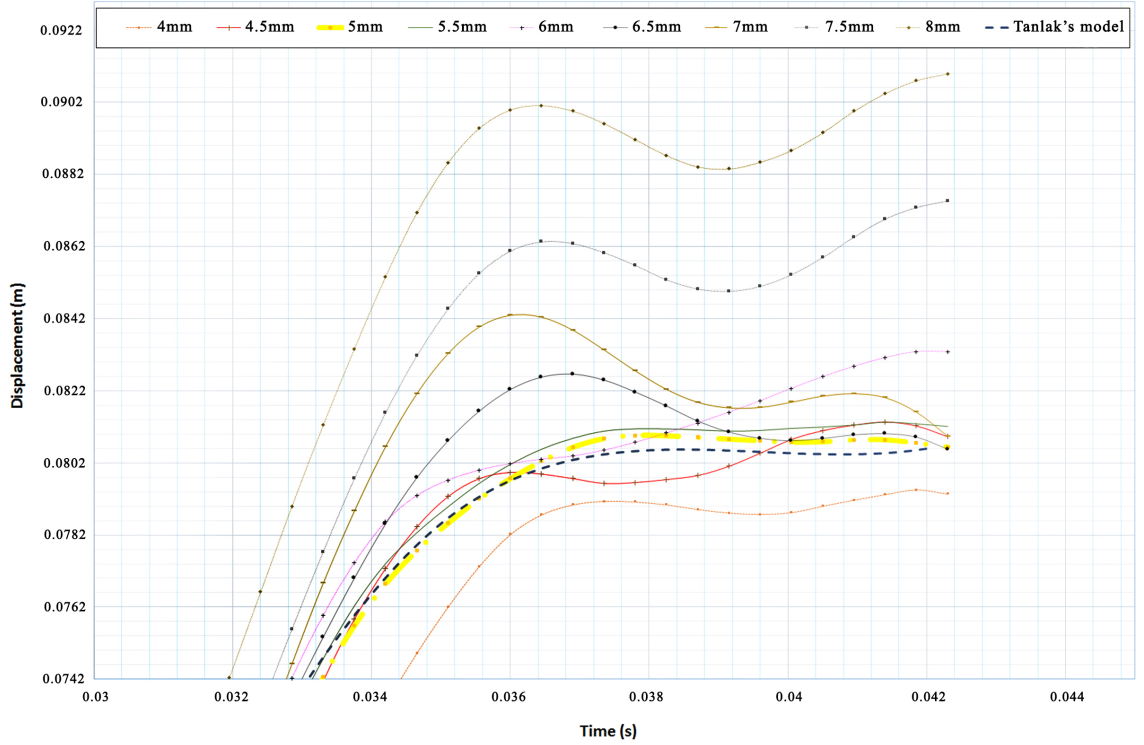


Figure 6.1. The convergence result of several mesh size.

6.2. Model Validation

In the absence of experimental data, the model developed in the present study is validated by comparing its predictions with that of a previous study. Tanlak [34] using ABAQUS, modeled the structural response of a bumper beam and crash box in a standard low-velocity collision test, RCAR (Research Council for Automobile Repairs [55]), which has the same test conditions as IIHS [56]. Figure 6.2 shows the models of Tanlak and the present study. The rigid barrier is made of steel material with $100 \text{ mm} \pm 2 \text{ mm}$ height, $1500 \text{ mm} \pm 25 \text{ mm}$ width, and $3404 \text{ mm} \pm 25 \text{ mm}$ radius of curvature cross its full width. The test is done at a speed of $2.78 \frac{\text{m}}{\text{s}}$ ($10 \frac{\text{km}}{\text{h}}$). AA6061-

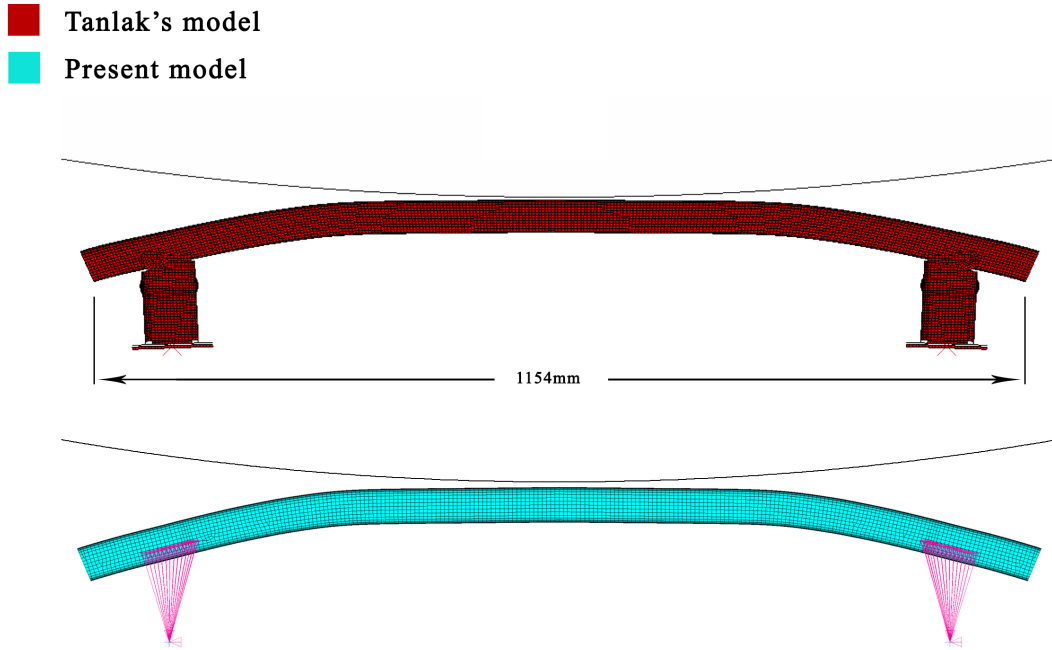


Figure 6.2. Schematic view of bumper beam for Tanlak's model [62] and the present model.

T6 Aluminum is selected for the material of the bumper beam. Its thickness is 2.5 mm and length is 1154 mm. It has a rectangular cross-sectional shape with dimensions $50 \times 76 \text{ mm}^2$. The mass attached to the rigid back end plates of crash-boxes are 550 kg each (totally 1100 kg, representing the mass of the vehicle and the driver). The model developed by Tanlak [62] includes crash boxes as well, while in the present model they

are excluded to save computational time. The mass points are directly attached to the rear of the bumper beam.

The model developed in this study is used to simulate the same impact conditions for the same bumper geometry without crash boxes. Figure 6.3 shows the deformed shapes of the bumper beams at a time when the velocity of the crash boxes becomes zero. The deformed shapes and the displacements of the bumper models are quite similar. As seen in Figure 6.3 the displacement profiles are very similar.

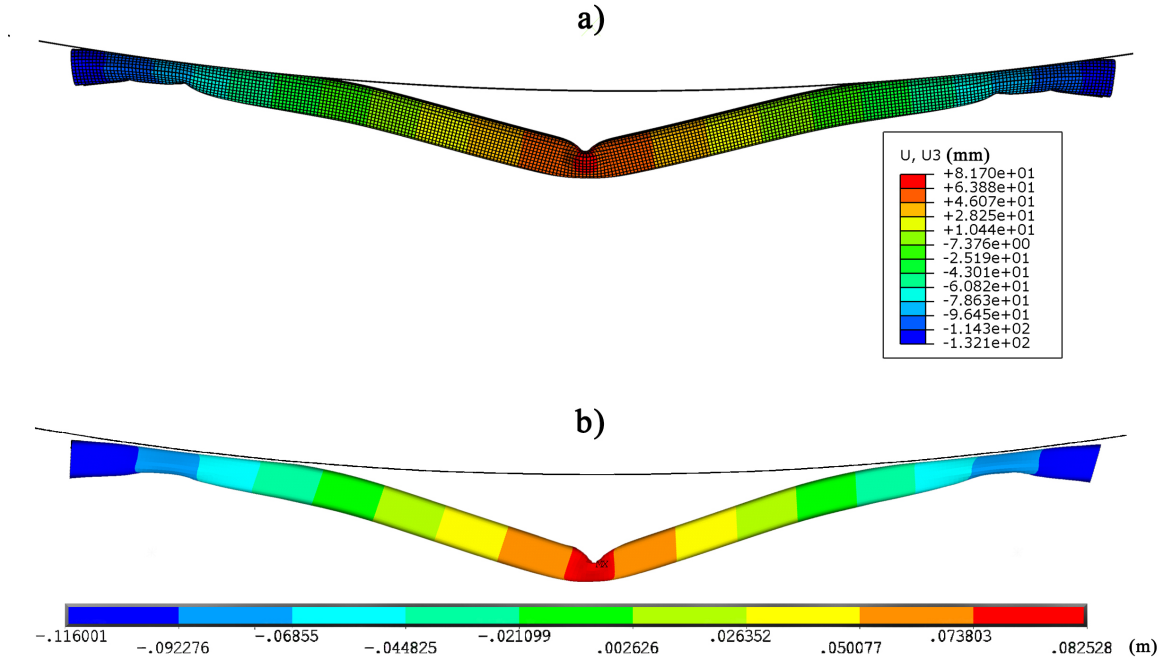


Figure 6.3. Displacement contour plots of bumper beam in velocity direction obtained by a) Tanlak's model [62], b) the present model.

Figure 6.4 presents the displacement of the same center foremost node of bumper beams obtained by both models as a function of time. The first contact occurs at 0.0028 sec. The foremost points get separated at about 0.011 sec. The displacements of both nodes reach their maximum value at about 0.04 sec. The bumper models become separated from the barrier at about 0.075 sec, when the mass points start to speed up in the reverse directions.

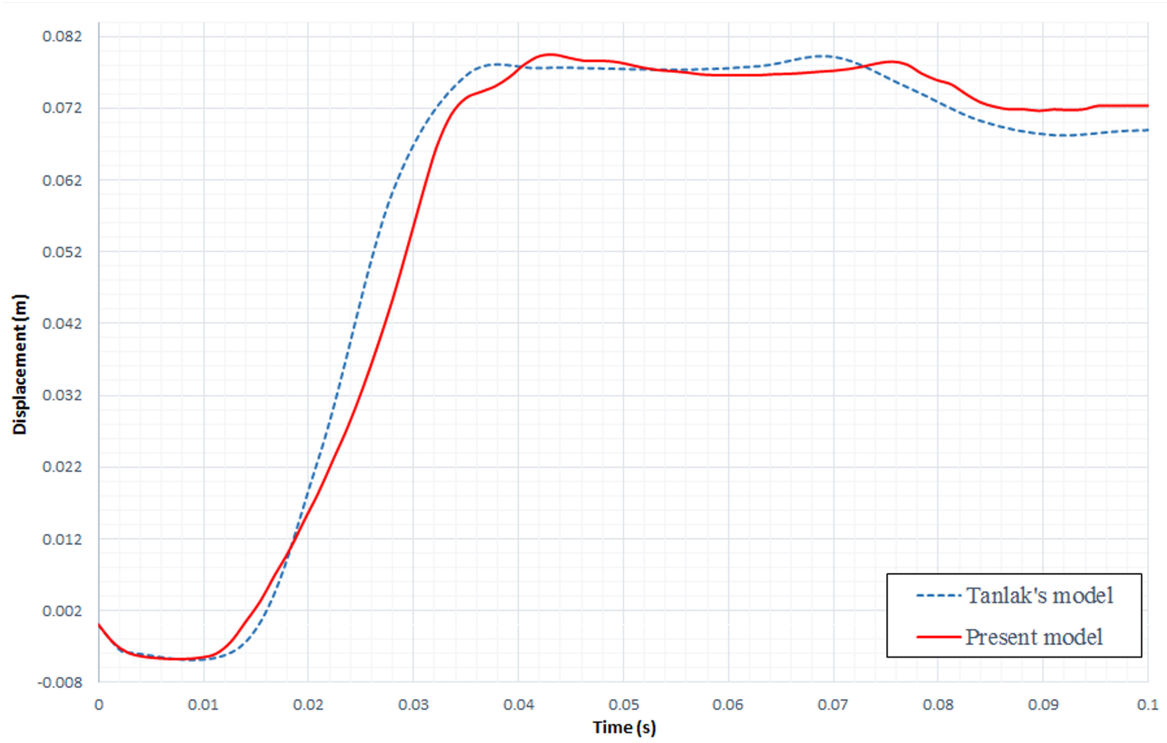


Figure 6.4. The displacement versus time of the foremost nodes of the two models .

Figure 6.5 shows the undeformed configuration of the crash boxes, their final plastic dissipation energy and strain energy distributions. Significant portion of the crash boxes does not undergo plastic deformation; a small portion is plastically bent, which may be avoided with a more proper design. Because crash boxes mainly deforms elastically, compared to the strain energy absorbed by the bumper beam, the crash boxes absorb a small amount of the impact energy. For this reason, one may assume that neglecting deformation of crash boxes does not lead to an appreciable error in evaluating the deformation behavior of the bumper beam.

Figure 6.6 and 6.7 show the energy results obtained by the two models. After the kinetic energy becomes equal to zero, the vehicle springs back from the barrier. As can be seen in the figures, the separation times obtained by the two models are close to each other and the variations in the energy levels also correlate well.

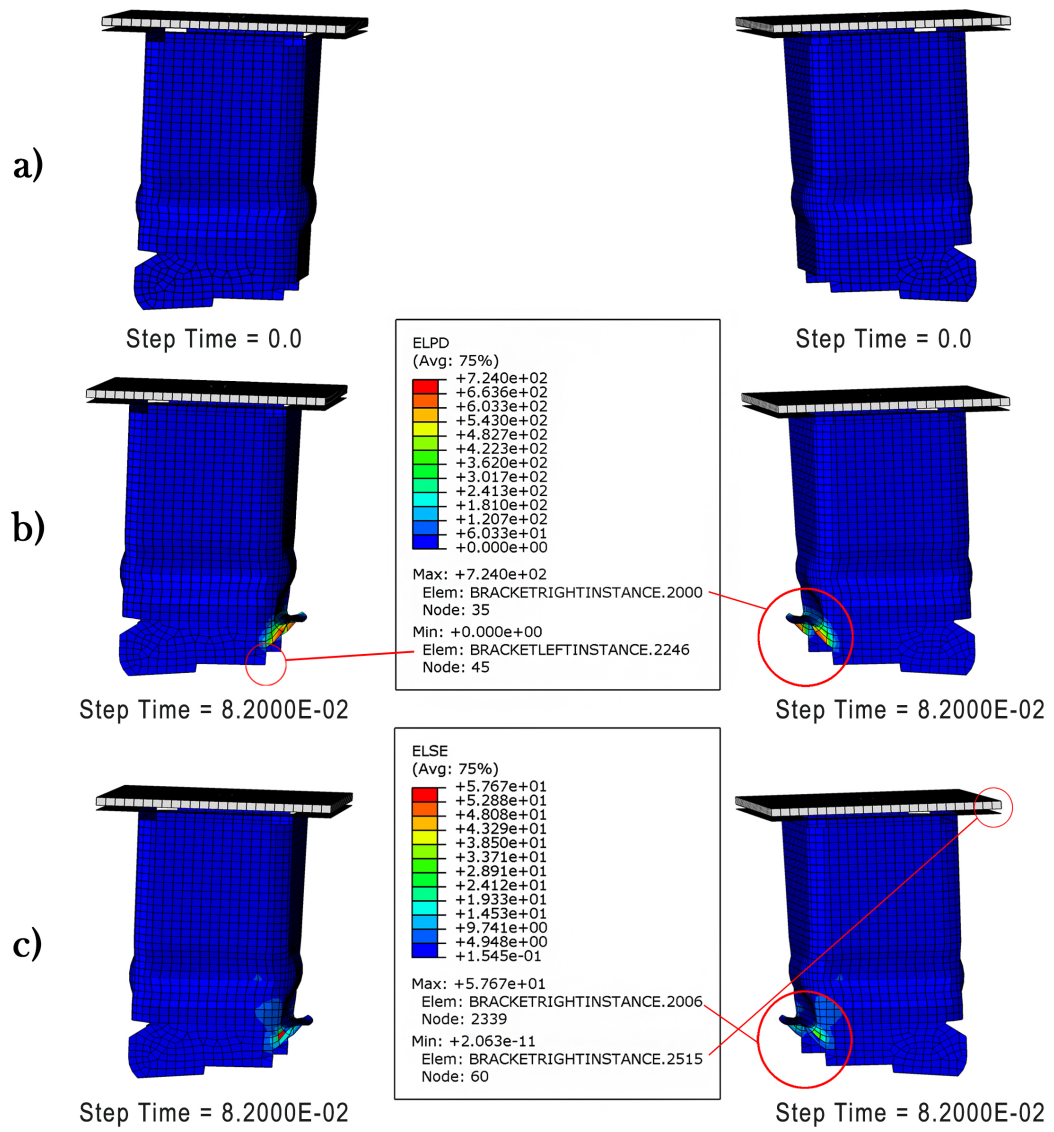


Figure 6.5. (a) Initial configurations. (b) Plastic dissipation energy magnitude at 8.2ms . (c) Strain energy magnitude at 8.2ms. [62]

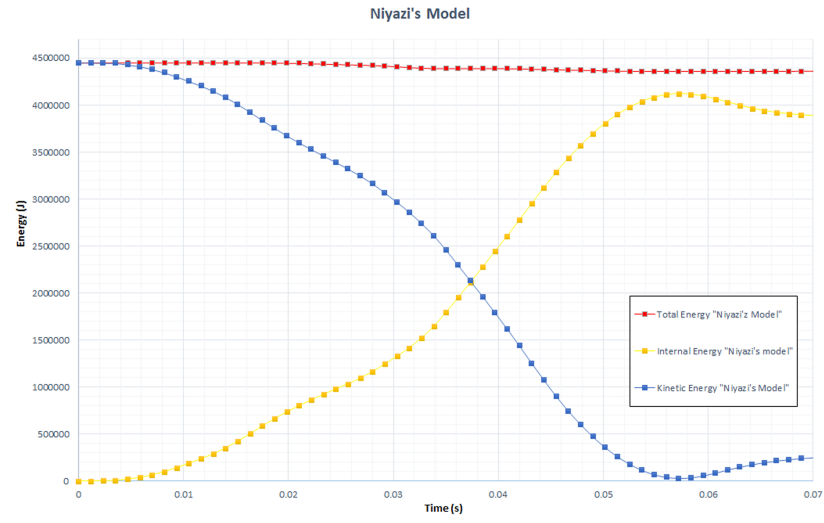


Figure 6.6. Energy diagram obtained by Tanlak's model. [62]

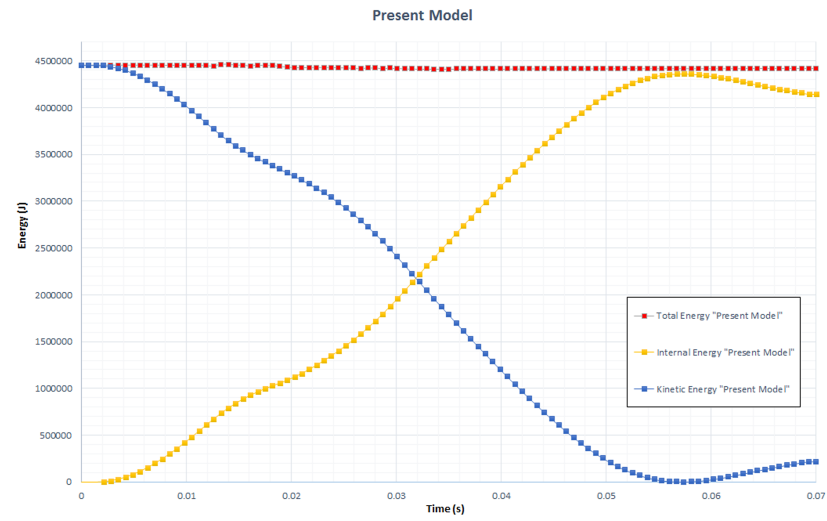


Figure 6.7. Energy diagram for present study.

6.3. Results

The optimization problem is solved to find the best shape using a hybrid-optimization algorithm. To begin with, the relative weights of the terms in the objective function are decided by choosing $c_1 = 1$ and $c_2 = 5$ in Eq. 5.2, which means that, c_2 coefficient of intrusion is five times more important than that of weight. Then, the optimum shapes for steel and aluminum bumpers are obtained using MSA algorithm. In order to ensure the convergence of the optimum shape, iterations are continued with Nelder-Mead algorithm. As shown in Figure 6.8, there are three benchmark shapes and two optimum shapes for steel and aluminum materials.


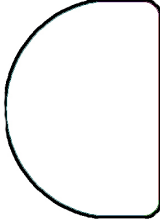

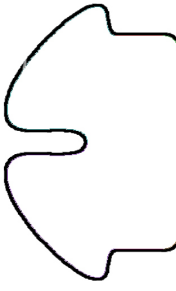
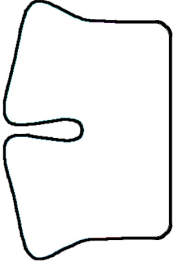
BENCHMARKS			OPTIMUM SHAPES	
Rectangle	Dome	Currently in use	Best Shape (St)	Best Shape (Al)
				

Figure 6.8. The benchmark and optimum shapes.

The main design goal of bumper beam design according to the requirements for low-velocity impacts is to reduce damage to the expensive parts of the vehicle behind the bumper beam such as radiator. As there is no limitation and regulation for how much the bumper beam can deform, as explained in chapter 5, the intrusion is defined to check if the back-middle of the bumper beam deflects beyond the acceptable region or not. In order to compare different designs of the bumper beam, the intrusion-mass ratio (RIM) of the bumpers with different mass is defined as

$$R_{IM} = \frac{I}{m} \quad (6.1)$$

where m is the mass of the bumper beam and I is the intrusion of the bumper beam which is defined as the change in the distance between the mass points (back end of the crash boxes) and the back-middle of the bumper beam. Figure 6.9 shows that a low

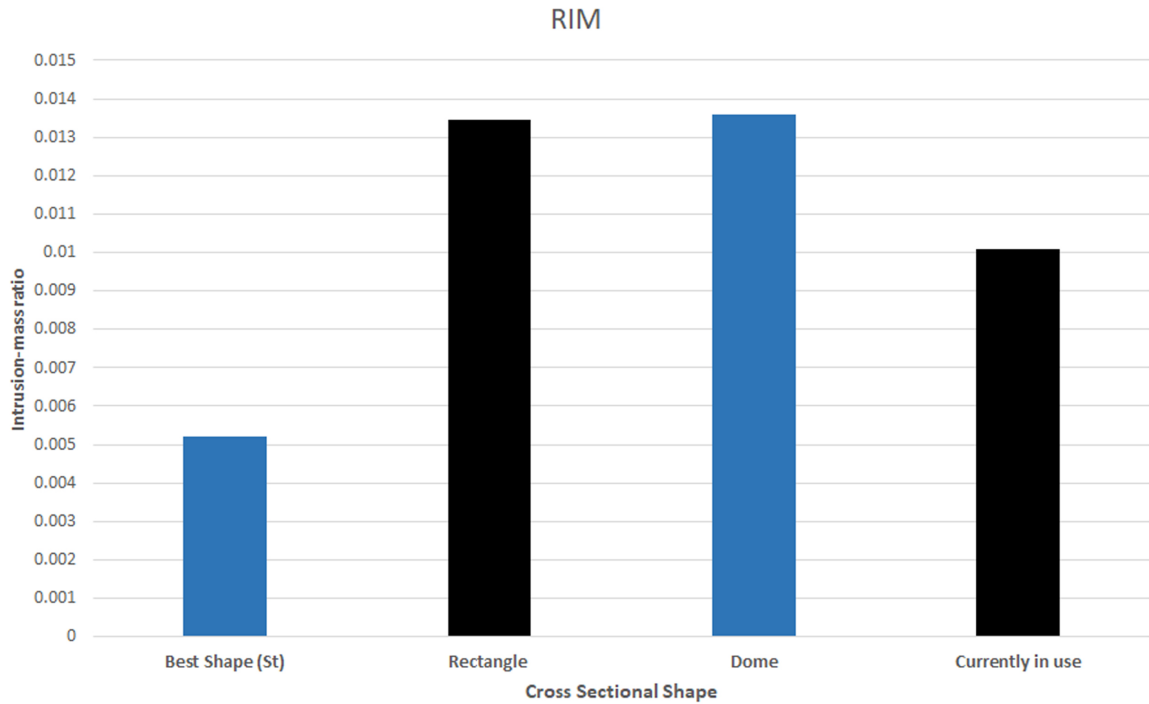


Figure 6.9. The intrusion-mass ratio of the steel bumper beams.

value of R_{IM} indicates a safer bumper beam, because the intrusion value of the best shape is 44.56mm lower than the best of the benchmark shapes in the same thickness situation.

On the other hand, the intrusion of the same bumper beams is compared in equal mass situation as shown in Figure 6.10. The results show that, the intrusion of the best-shaped steel beam (54.86mm) is 28.45 mm lower than that of currently-in-use model (83.31mm). Hence by decreasing the thickness of the best shape model, the weight of the bumper beam will decrease without exceed the limiting of intrusion which is 83.31mm. Figure 6.11 shows the intrusion of various thicknesses of best shape (St). By selecting the 1.9 mm thickness, the intrusion value will be 81.13 mm which is better than that of the currently-in-use model. So, the weight of the bumper beam is reduced by 25.28 % in comparison to the currently-in-use model. As described in

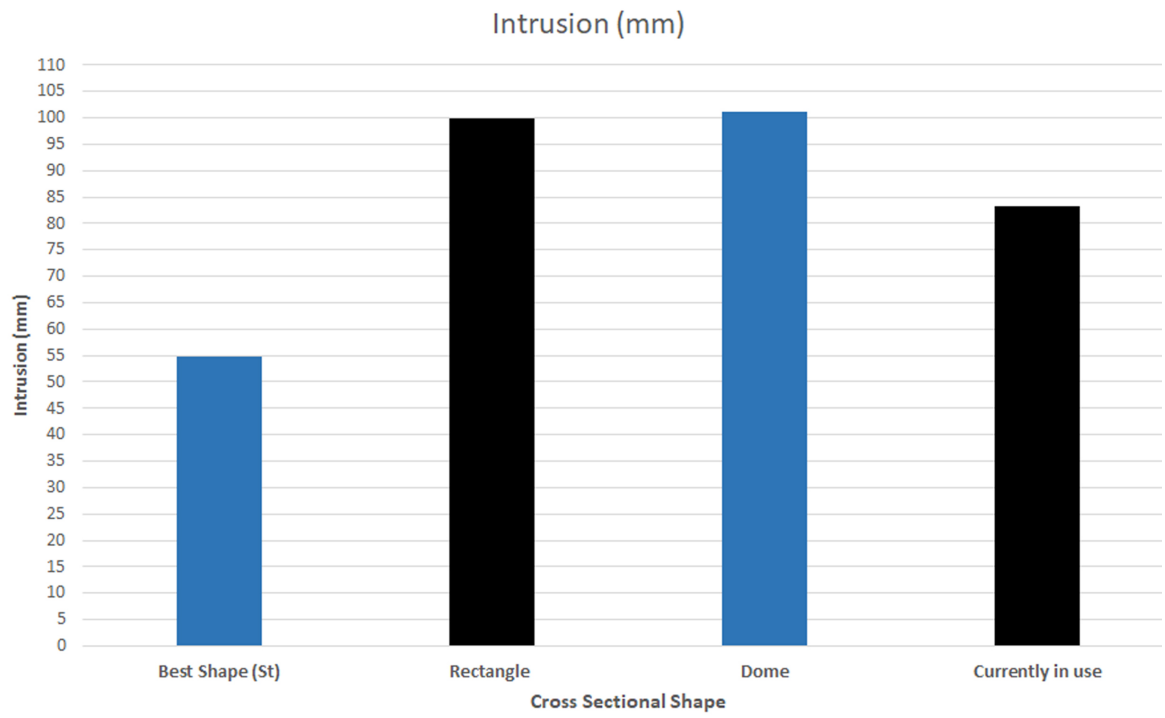


Figure 6.10. The intrusion of the steel bumper beams in a same weight situation.

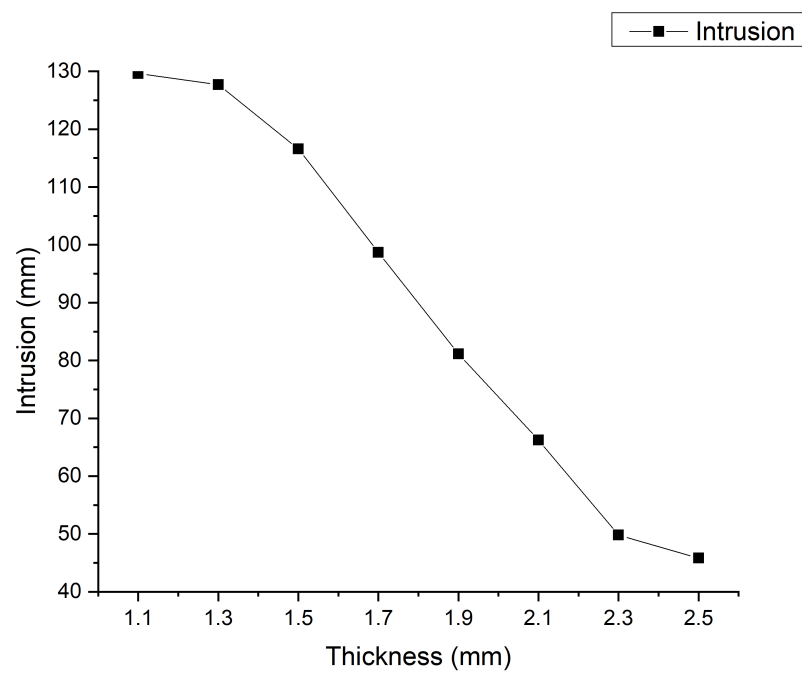


Figure 6.11. The intrusion of the steel bumper beams in various thicknesses.

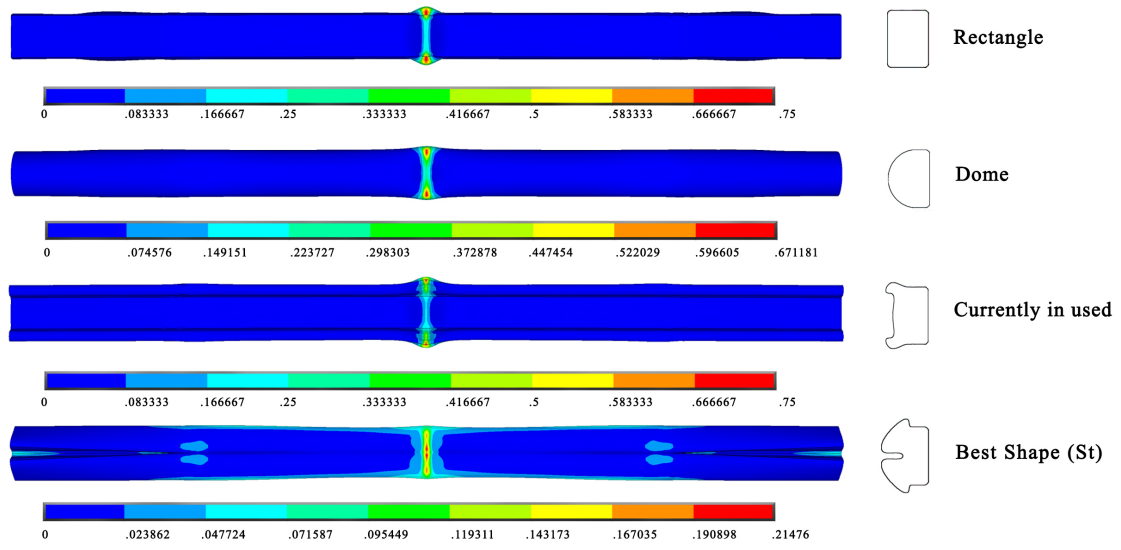


Figure 6.12. The contour of equivalent plastic strain of the steel bumper beams.

the standard of low-velocity impact, besides having a low intrusion and being in a safe region, bumper beams should not undergo extreme plastic strain, which leads to rupture in the bumper beam. Figure 6.12 shows that the best shape has the lowest equivalent plastic strain among all shapes.

In Figure 6.13, the energy versus time curves of the total system is shown. The total energy of the system, which is about $4.4\text{e}03$ J is the same for all bumper beams having same thicknesses. As the bumper beam hits the barrier, the kinetic energy of the bumper beam transforms into deformation energy, which leads to an increase in the absorbed energy of the bumper beam.

As seen in Figure 6.13, the absorption energy reaches its peak value at different times for different shapes with the same thicknesses due to the differences in their deformation behavior. The energy absorption capacity at time $8\text{e}-02$ sec is about $3.7\text{e}3$ J for best shape which is due to the permanent plastic deformation. This is larger than that of the benchmark shapes. This means the energy absorbing capacity of the optimum shape is better than the others.

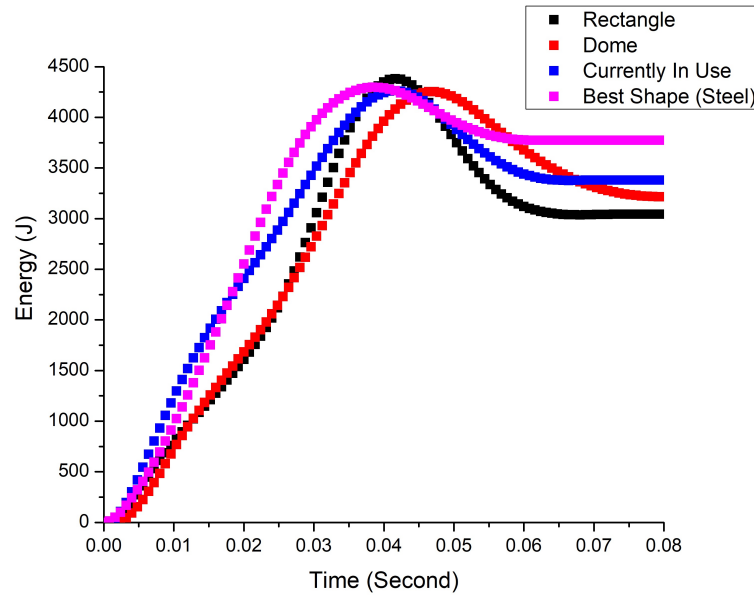


Figure 6.13. The energy absorption of the steel bumper beams in a same thickness situation.

In the full frontal low-velocity impact, the middle of the bumper beam is considered as a critical region, where the first contact occurs with the rigid barrier. The critical region of the bumper beam is a place where plastic hinge and the largest bending moment can develop. In the beams like rectangle and dome shaped cross-section, which have low flexural stiffness, once the bumper hits the rigid wall, a plastic hinge begins to develop. So, occurrence of plastic hinge partly relates to the poor performance of the beams. As can be seen in Figure 6.14, the optimum steel beam does not suffer any plastic hinge and deformation is more uniformly distributed.

The bumper beam designed for low-velocity impact should also satisfy the high-velocity impact performance criteria. Peak transmitted force at high-velocity impacts is one of the parameters considered in vehicle design. The peak transmitted force should be as low as possible to decrease the jerking effect felt by occupants during a crash so that neck injury can be avoided. In this thesis, peak forces transmitted at high-velocity impact are also compared. Impact velocity is 56km/h as in EURO-NCAP standard tests [64]. Figure 6.15 shows that the best shape has peak force about 200kN, which is the minimum value among all shapes.

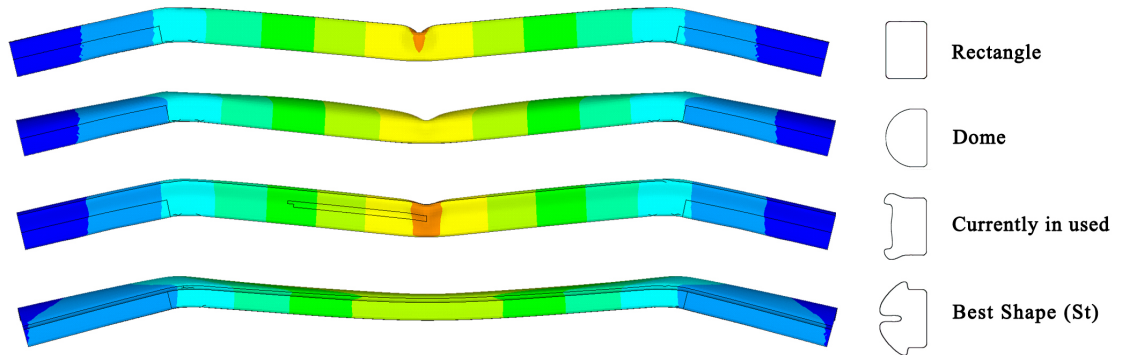


Figure 6.14. The presence of the plastic hinge in steel bumper beams.

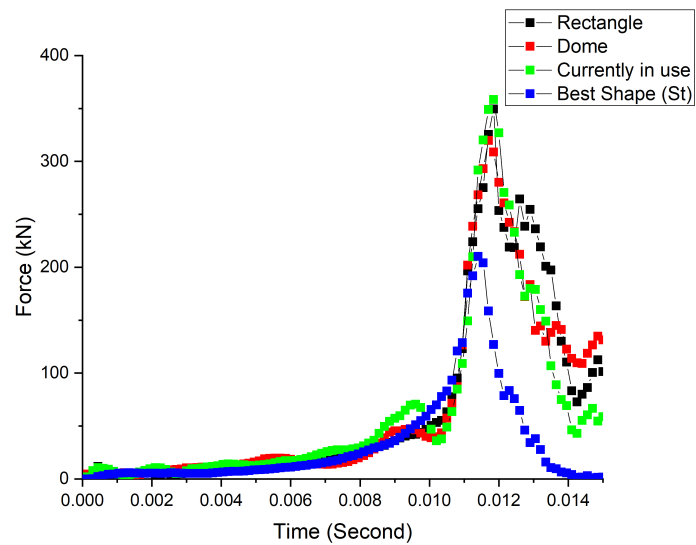


Figure 6.15. The peak transmitted force at high-velocity impacts for different-shaped beams having the same weight.

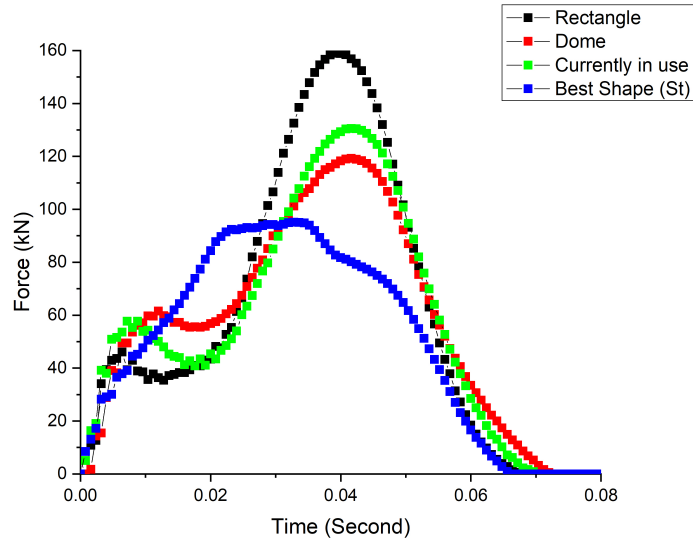


Figure 6.16. The peak transmitted force at low-velocity impacts for same weight situations .

Figure 6.16 shows the peak forces transmitted through different bumper designs having the same weight. The peak force of the best shape is about 92 kN, which is the lowest one compared to the benchmark shapes. In both low and high-velocity collisions, the best shape shows a better performance regarding peak force.

The results show that the best shape obtained using steel material has better performance in case of intrusion, equivalent plastic strain, energy absorption capacity and peak transmitted force in comparison with the benchmark shapes. Besides, the optimum shape is obtained for aluminum material. Since the benchmark shapes show quite low performance, the optimum shape of aluminum is directly compared with steel having the same weight to see which one is better suited as bumper material. Figure 6.17 shows that the optimum steel shape of steel absorbs about 3.91×10^3 J energy, while, this value is 3.22×10^3 J for the optimum aluminum shape.

As can be seen in Figures 6.18, the optimum steel shape shows a better performance in comparison to the optimum aluminum shape in case of peak transmitted force which is about 90 kN.

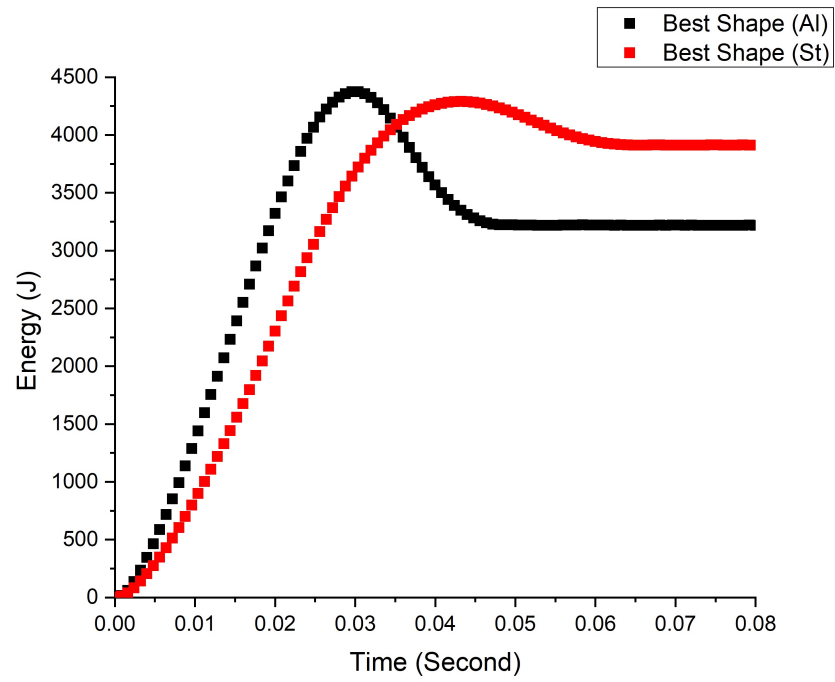


Figure 6.17. The Energy absorption of the best shapes in same weight situation.

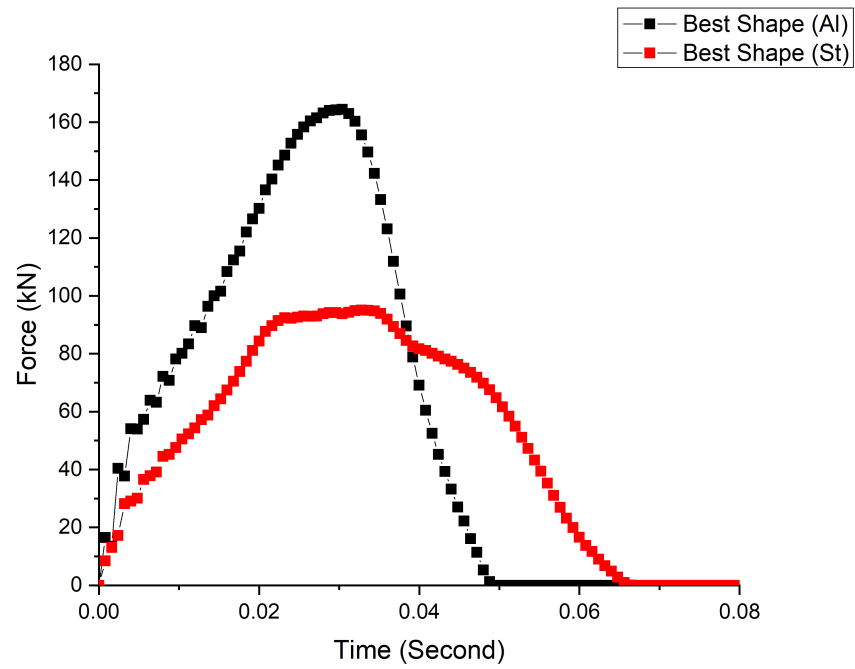


Figure 6.18. The peak transmitted force at low-velocity impacts for the best shapes in same weight situations.

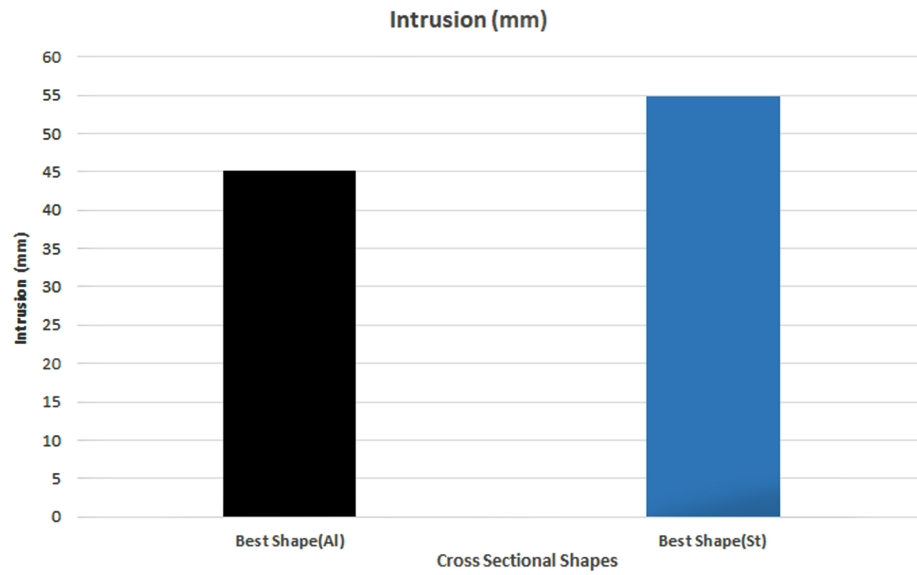


Figure 6.19. The intrusion of the best shapes having same weight.

The comparison of the intrusion for best optimum shapes shows that, the optimum shape of aluminum has better intrusion than optimum shape of steel. As can be seen in Figure 6.19, the value of intrusion for aluminum is about 45mm where steel has intrusion about 55mm.

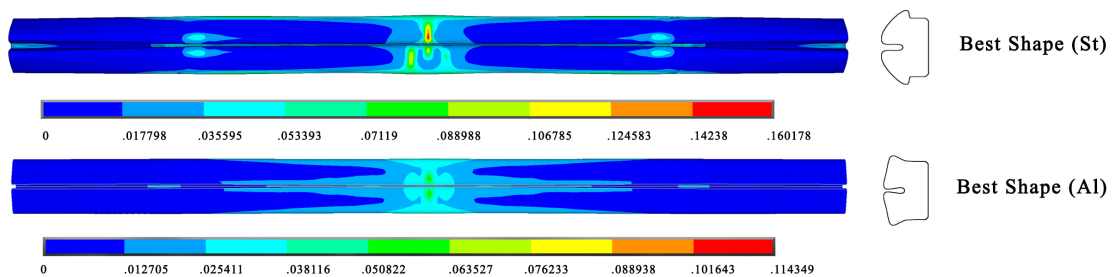


Figure 6.20. The contour of equivalent plastic strain of the steel and aluminum best shapes.

Figure 6.20 shows a similar behaviour in equivalent plastic strain. The maximum plastic strain of steel is larger, but concerning that low-carbon steel is more ductile than the aluminum alloy, one can assume that both beams will preserve their integrity during low-velocity impacts.

Optimum shape of steel, despite having good performance in case of peak transmitted force and energy, has intrusion higher than the optimum aluminum shape. Since, optimum shape of steel successfully satisfied the limitation of the intrusion, and having cost lower than aluminum material, it is recommended to be used as a bumper beam material in this study.

7. FUTURE WORKS AND RECOMMENDATIONS

In this study, by optimally designing the cross-sectional shape of a bumper beam, improvements are obtained in impact performance like peak-transmitted force, intrusion, and absorbed energy. Despite having improved the bumper beam design, there are potential improvements that can be done. The parameters like thickness, radius of curvature of the beam, dimensions of the cross-section are important design parameters affecting the performance of the bumper beam. Finding optimal values for these design variables may further improve the performance of the beam. Besides, the material properties such as yield stress and elastic modulus significantly affect the performance, so, selecting materials with high strength-to-weight ratio can help in a way to reach a lightweight structure. Among those materials, carbon-fiber composites and the hybrid materials can be mentioned. Besides the structure of the beam can be improved by selecting a hybrid structural design.

8. CONCLUSIONS

This thesis study focuses on improving the performance of a bumper beam by optimizing its cross-sectional shape. A standard low-velocity impact test, IIHS, is simulated to determine the response of the beam during impact. In the optimization procedure, the shape of the cross-section is defined by spline curves passing through key points. Some of the key points are allowed to move in a limited region called search domain. The coordinates of these key points are taken as optimization variables. The barrier size, contact radius, and the collision velocity are taken the same as the standards. The bumper beam is modeled as a deformable body; the rest of the vehicle parts are taken as rigid and their effects are taken into account by defining mass points. These mass points are rigidly coupled to the back end of the bumper beam. In order to reduce the computational time of optimization, explicit dynamic analysis is carried out with shell elements. Optimum shapes are obtained for two different materials, an aluminum and a steel. A number of benchmark shapes are selected for comparison, dome shaped and rectangular cross-sections, and a shape currently in use in a commercial car. The performances of the optimum shapes and the benchmark shapes are compared in terms of maximum intrusion, maximum plastic strain, peak-transmitted force, absorbed energy, weight, and cost.

Different optimal shapes are obtained for an aluminum alloy and a low-carbon steel. Therefore, optimization process should be repeated when another candidate material is considered. Optimal shapes are expected be different for different thicknesses; but within the scope of the thesis, optimal shapes for different thicknesses were not obtained.

The optimal shapes show significantly improved performance over the benchmark shapes in terms of all criteria. The maximum intrusion is less than at least 25 mm compared to the benchmark shapes having the same weight. The maximum plastic strain is much lower; so the structural integrity of the bumper beams with optimal cross-sectional shape is expected to be preserved during a low velocity collision as

opposed to the benchmark shapes. Because deformation is more uniform in optimal beams, a larger portion of the impact energy is absorbed. Peak transmitted forces under both low and high-velocity collisions are much lower.

Optimal aluminum bumper beam shows a better performance compared to the steel one having the same weight in terms of intrusion, but a lower performance in terms of absorbed energy. Considering that, the differences in performance are not significant and aluminum is much costly, low-carbon steel is a better alternative as a bumper beam material.

REFERENCES

1. Australian Transport Safety Bureau, “Road Safety in Australia: A Publication Commemorating World Health Day 2004”, pp. 1–335.
2. Sapuan, S. M., M. A. Maleque, M. Hameedullah, M. N. Suddin and N. Ismail, “A note on the conceptual design of polymeric composite automotive bumper system”, *Journal of Materials Processing Technology*, Vol. 159, No. 2, pp. 145–151, 2005.
3. Luda, M. P., V. Brunella and D. Guaratto, “Characterisation of Used PP-Based Car Bumpers and Their Recycling Properties”, *ISRN Materials Science*, Vol. 2013, No. March, p. 12, 2013.
4. Dange, M. V., R. B. Buktar and N. R. Raykar, “Design and Analysis of an Automotive Front Bumper Beam for Low-Speed Impact”, *IOSR Journal of Mechanical and Civil Engineering Ver*, Vol. 12, No. 2, pp. 2320–334, 2015.
5. Johnson, W. and A. C. Walton, “An experimental investigation of the energy dissipation of a number of car bumpers under quasi-static lateral loads”, *International Journal of Impact Engineering*, Vol. 1, pp. 301–308, 1983.
6. Zhang, Z., S. Liu and Z. Tang, “Design optimization of cross-sectional configuration of rib-reinforced thin-walled beam”, *Thin-Walled Structures*, Vol. 47, No. 8-9, pp. 868–878, 2009.
7. A.a, H., S. M.S.a, I. N.a and N. Y.b, “Material selection of polymeric composite automotive bumper beam using analytical hierarchy process”, *Journal of Central South University of Technology (English Edition)*, Vol. 17, No. 2, pp. 244–256, 2010.
8. Hosseinzadeh, R., M. M. Shokrieh and L. B. Lessard, “Parametric study of automotive composite bumper beams subjected to low-velocity impacts”, *Composite*

- Structures*, Vol. 68, No. 4, pp. 419–427, 2005.
9. Marzbanrad, J., M. Alijanpour and M. S. Kiasat, “Design and analysis of an automotive bumper beam in low-speed frontal crashes”, *Thin-Walled Structures*, Vol. 47, No. 8-9, pp. 902–911, 2009.
 10. Wang, T. and Y. Li, “Design and analysis of automotive carbon fiber composite bumper beam based on finite element analysis”, *Advances in Mechanical Engineering*, Vol. 7, No. 6, pp. 1–12, 2015.
 11. ECE, *Uniform Provisions Concerning the Approval of Vehicles With Regard To Their Front and Rear Protective Devices (Bumpers, Etc.)*, Tech. Rep. March, 1980.
 12. Kokkula, S., M. Langseth, O. S. Hopperstad and O. G. Lademo, “Behaviour of an automotive bumper beam-longitudinal system at 40% offset impact: An experimental and numerical study”, *Latin American Journal of Solids and Structures*, Vol. 3, No. 1, pp. 59–73, 2006.
 13. Farkas, L., D. Moens, S. Donders and D. Vandepitte, “Optimisation study of a vehicle bumper subsystem with fuzzy parameters”, *Mechanical Systems and Signal Processing*, Vol. 32, 2012.
 14. Cheon, S. S., J. H. Choi and D. G. Lee, “Development of the composite bumper beam for passenger cars”, *Composite Structures*, Vol. 32, No. 1-4, pp. 491–499, 1995.
 15. Belingardi, G., A. T. Beyene and E. G. Koricho, “Geometrical optimization of bumper beam profile made of pultruded composite by numerical simulation”, *Composite Structures*, Vol. 102, pp. 217–225, 2013.
 16. Li, M., Z. Xia and W. Shangguan, “Analysis and Simulation of Low-Speed Collision of Car Front Bumpers”, *SAE Technical Paper 2018-01-1460*, 2018, pp. 1–9, 2018.

17. Mo, F., S. Zhao, C. Yu, Z. Xiao and S. Duan, “Design of a Conceptual Bumper Energy Absorber Coupling Pedestrian Safety and Low-Speed Impact Requirements”, *Applied Bionics and Biomechanics*, Vol. 2018, 2018.
18. Yim, H. J., M.-s. Kim, J. Park, S.-j. Heo and D. K. Park, “Shape Optimization of Bumper Beam Cross Section for Low Speed Crash”, *SAE International*, Vol. 7, No. 724, p. 2, 2009.
19. Sonawane, C. R. and A. L. Shelar, “Strength Enhancement of Car Front Bumper for Slow Speed Impact by FEA Method as per IIHS Regulation”, *Journal of The Institution of Engineers (India): Series C*, 2017.
20. Shin, M.-K., S. I. Yi, O.-T. Kwon and G.-J. Park, “Structural optimization of the automobile frontal structure for pedestrian protection and the low-speed impact test”, *Proceedings of The Institution of Mechanical Engineers Part D-journal of Automobile Engineering - Proc Inst Mech Eng. D-J AUTO*, Vol. 222, pp. 2373–2387, 2008.
21. Sampath Rao, P., “Design Analysis of Bumper Beam Subjected To Offset Impact Loading for Automotive Applications”, *International Journal of Mechanical Engineering and Technology*, Vol. 6, No. 5, pp. 976–6340, 2015.
22. Frank, T. and K. Gruber, “Numerical simulation of frontal impact and offset collisions”, *CRAY Channels, Cray Research Inc*, pp. 2–6, 1992.
23. M. Patel, N., C. Penninger and J. E. Renaud, “Topology Synthesis of Extrusion-Based Nonlinear Transient Designs”, *Journal of Mechanical Design - J Mechanical Design*, Vol. 131, 2009.
24. Zarei, H. R. and M. Kröger, “Bending behavior of empty and foam-filled beams: Structural optimization”, *International Journal of Impact Engineering*, Vol. 35, No. 6, pp. 521–529, 2008.

25. Agar, P. S. U. S. and D. R. K. K. Amalakkannan, “Performance Enhancement of a Car Bumper using Crash Analysis”, Vol. 09, No. 06, pp. 769–772, 2017.
26. Doruk, E., “Steel processing effects on crash performance of vehicle safety related applications”, Vol. 3, pp. 351–358, 2017.
27. Simon, P. and P. Beggs, “A numerical performance comparison of a dual-phase steel and aluminium alloy bumper bar system”, *International Journal of Crashworthiness*, Vol. 15, No. 4, pp. 425–442, 2010.
28. Kashinath, K. S. and C. A. Balasaheb, “Review of Design & Analysis of Bumper Beam in Low Speed Frontal Crashes”, *International Journal of Industrial Electronics and Electrical Engineering*, Vol. 3, No. December, pp. 56–63, 2013.
29. Sun, G., T. Pang, C. Xu, G. Zheng and J. Song, “Energy absorption mechanics for variable thickness thin-walled structures”, *Thin-Walled Structures*, Vol. 118, No. April, pp. 214–228, 2017.
30. Norhidayah, M., A. A. Hambali, Y. M. Yuhazri, M. Zolkarnain, Taufik and H. Saifuddin, “A Review of Current Development in Natural Fiber Composites in Automotive Applications”, *Applied Mechanics and Materials*, Vol. 564, No. October, pp. 3–7, 2014.
31. Farkas, L., C. Canadas, S. Donders, H. Van Der Auweraer and D. Schildermans, “Optimization study of a parametric vehicle bumper subsystem under multiple load cases”, *Recent Advances in Optimization and its Applications in Engineering*, pp. 481–490, 2010.
32. Duponchee, G Tilley, D., “Topological optimization of a bumper beam via the messy genetic algorithm”, *ProQuest Science Journals pg. 133 Reproduced*, Vol. 2, No. 212, p. 133, 1998.
33. Müllerschön, H., N. Lazarov and K. Witowski, “Application of Topology Optimiza-

- tion for Crash with LS-OPT ® / Topology”, *11th International LS-DYNA Users Conference*, Vol. 11, No. 2, pp. 39–46, 2010.
34. Tanlak, N., F. O. Sonmez and M. Senaltun, “Shape optimization of bumper beams under high-velocity impact loads”, *Engineering Structures*, Vol. 95, No. October 2017, pp. 49–60, 2015.
 35. Wang, D., S. Zhang, C. Wang and C. Zhang, “Structure-material-performance integration lightweight optimisation design for frontal bumper system”, *International Journal of Crashworthiness*, Vol. 23, No. 3, pp. 311–327, 2018.
 36. Enriquez, J., *Body in white architecture for an electric vehicle concept*, Ph.D. Thesis, Chalmers University of Technology, 2016.
 37. Deb, A., A. Naravane and E. C. Chirwa, “An offset rigid barrier-based test: Equivalence to the Insurance Institute for Highway Safety frontal offset impact safety test”, *International Journal of Crashworthiness*, Vol. 11, No. 4, pp. 281–290, 2006.
 38. Park, D. K., “A development of simple analysis model on bumper barrier impact and new IIHS bumper impact using the dynamically equivalent beam approach”, *Journal of Mechanical Science and Technology*, Vol. 25, No. 12, pp. 3107–3114, 2011.
 39. Kim, D. H., H. G. Kim and H. S. Kim, “Design optimization and manufacture of hybrid glass/carbon fiber reinforced composite bumper beam for automobile vehicle”, *Composite Structures*, Vol. 131, 2015.
 40. C. Jacob, G., J. F. Fellers, S. Simunovic and J. Michael Starbuck, “Energy Absorption in Polymer Composites for Automotive Crashworthiness”, *Journal of Composite Materials - J Composite Material*, Vol. 36, pp. 813–850, 2002.
 41. Chen, H., Y. Yang and L. Wang, “Vehicle front structure energy absorbing optimization in frontal impact”, *Open Mechanical Engineering Journal*, Vol. 9, No. 1,

- pp. 168–172, 2015.
42. Jiang, L. and H. Hu, “Finite element modeling of multilayer orthogonal auxetic composites under low-velocity impact”, *Materials*, Vol. 10, No. 8, 2017.
 43. Xiao, Z., J. Fang, G. Sun and Q. Li, “Crashworthiness design for functionally graded foam-filled bumper beam”, *Advances in Engineering Software*, Vol. 85, pp. 81–95, 2015.
 44. The-Blueprints.com, *Evolution Graphics B.V.*, 2011, <https://www.the-blueprints.com>, accessed at December 2018.
 45. Insurance Institute for Highway Safety, *IIHS low-speed crash test (goals of the new program)*, Tech. Rep. May, 2006.
 46. National Highway Traffic Safety Administration (NHTSA), *Laboratory Test Procedure For New Car Assessment Program Frontal Impact Testing*, Tech. Rep. September, 2012.
 47. Sadd, M. H., *Elasticity*, University of Rhode Island, Rhode Island Amsterd, 2005.
 48. University, A., *Crash Analysis with RADIOSS – A Study Guide*, 2018.
 49. C., H. and M. A., “Determination of constitutive parameters from a Taylor test using inverse analysis”, *Strain*, Vol. 53, No. 6, p. e12249, 2017.
 50. Canonsburg, T. D., *ANSYS LS-DYNA User’s Guide*, Tech. Rep. April, 2009.
 51. Cowper, G. and P. Symonds, “Stain-hardening and strain-rate effects in the impact loading of cantilever beams”, *Distribution*, pp. 1–35, 1973.
 52. Abotula, S. and V. Chalivendra, “An experimental and numerical investigation of the static and dynamic constitutive behaviour of aluminium alloys”, *The Journal of Strain Analysis for Engineering Design*, Vol. 10, No. March 2016, p. 4, 2010.

53. Ansys Inc., *SHELL163 Element Description*, Tech. rep., 2017, help/ans_elem/Hlp_E_SHELL163.html.
54. Akbulut, M. and F. O. Sonmez, “Design optimization of laminated composites using a new variant of simulated annealing”, *Computers and Structures*, Vol. 89, No. 17-18, pp. 1712–1724, 2011.
55. *RCAR Low-speed structural crash test protocol*, Tech. Rep. 2, 2011.
56. IIHS, *Insurance Institute for Highway Safety Bumper Test and Rating Protocol (Version VIII)*, Tech. Rep. September, 2010.

APPENDIX A: HYBRID OPTIMIZATION ALGORITHM

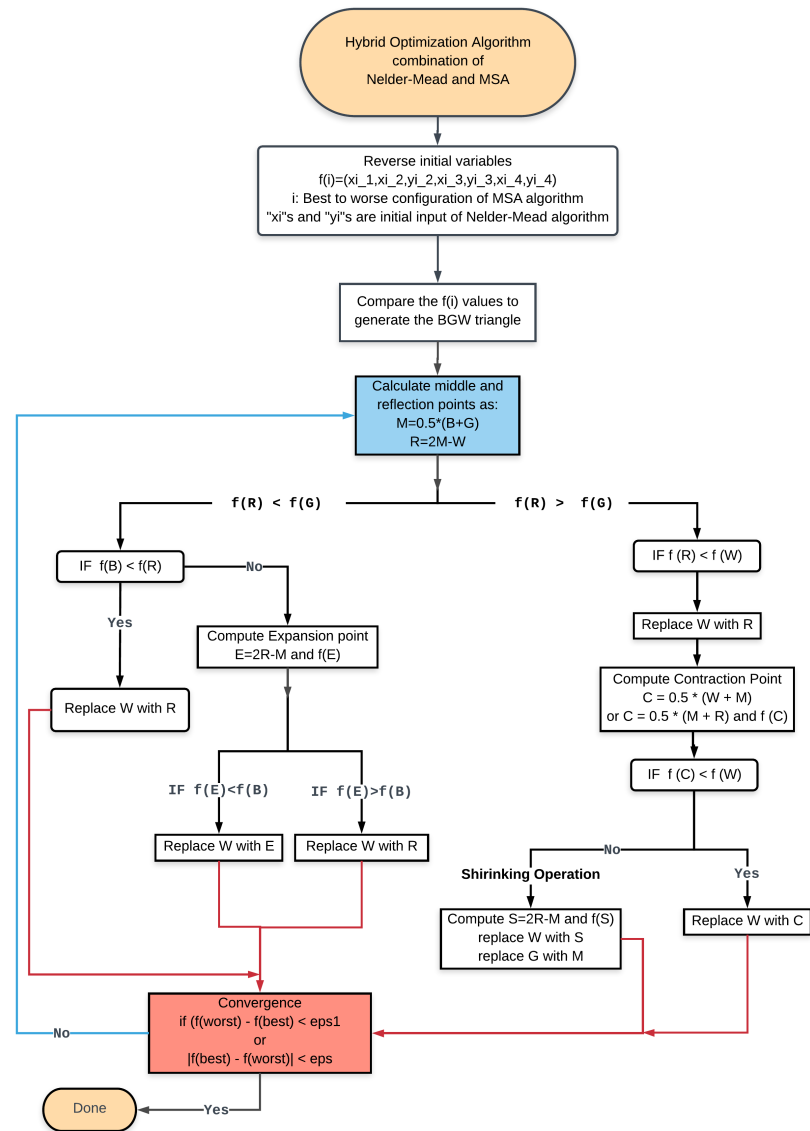


Figure A.1. The flow-chart of the hybrid-optimization algorithm